A novel *Smg6* mouse model reveals circadian clock regulation through the nonsense-mediated mRNA decay pathway

Georgia Katsioudi[1], René Dreos[1], Enes S. Arpa[1], Sevasti Gaspari[1], Angelica Liechti[1], Miho Sato[2], Christian H. Gabriel[3], Achim Kramer[3], Steven A. Brown[2], David Gatfield[1*]

[1] Center for Integrative Genomics, University of Lausanne, Lausanne, Switzerland

[2] Chronobiology and Sleep Research Group, Institute of Pharmacology and Toxicology, University of Zürich, Zürich, Switzerland

[3] Charité Universitätsmedizin Berlin, corporate member of Freie Universität Berlin, Humboldt-Universität zu Berlin, and Berlin Institute of Health, Laboratory of Chronobiology, Berlin, Germany

[*]corresponding author: david.gatfield@unil.ch

Short title: *NMD regulation of the mammalian circadian clock*

Abstract

Nonsense-mediated mRNA decay (NMD) has been intensively studied as a surveillance pathway that degrades erroneous transcripts arising from mutations or RNA processing errors. While additional roles in physiological control of mRNA stability have emerged, possible functions in mammalian physiology *in vivo* remain unclear. Here, we created a novel conditional mouse allele that allows converting the NMD effector nuclease SMG6 from wild-type to nuclease domain-mutant protein. We find that NMD downregulation affects the function of the circadian clock, a system known to require rapid mRNA turnover. Specifically, we uncover strong lengthening of free-running circadian periods for liver and fibroblast clocks, and direct NMD regulation of *Cry2* mRNA, encoding a key transcriptional repressor within the rhythm-generating feedback loop. Transcriptome-wide changes in daily mRNA accumulation patterns in the entrained liver, as well as an altered response to food entrainment, expand the known scope of NMD regulation in mammalian gene expression and physiology.

Teaser (125 characters):

NMD, an mRNA decay pathway with mostly quality control functions, has physiological roles in the mammalian circadian clock.

Introduction

Nonsense-mediated mRNA decay (NMD) is an important surveillance pathway to reduce gene expression errors that arise from mutations or mis-splicing and that are identified due to aberrant translation termination on “premature translation termination codons” (PTCs) (reviewed in (*1*)). In mammals, PTCs are recognised due to their position relative to an exon-junction complex (EJC), a multiprotein assembly that is deposited on mRNAs during splicing and removed from the transcript by the passage of translating ribosomes. Termination upstream of an EJC identifies the stop codon as aberrant, promoting the formation of an NMD factor complex comprising several UPF (up-frameshift) and SMG (suppressor with morphogenetic effects on genitalia) proteins. Briefly, interactions between UPF1, UPF2 and UPF3 proteins trigger UPF1 phosphorylation by the kinase SMG1. Phosphorylated UPF1 further recruits SMG5, SMG6 and SMG7, which are involved in executing the actual mRNA degradation step. Previous models suggested two distinct, redundant branches for decay involving SMG5-SMG7 (that can recruit general, non-NMD-specific exonucleases) or SMG6 (an NMD-specific endonuclease). Recent evidence, however, argues for mechanistic overlap (*2*). A linear pathway involving decay “licensing” through SMG5-SMG7 followed by SMG6-mediated endonucleolytic cleavage has been proposed as the main mechanism of mRNA decay (*3*).

Early transcriptome-wide analyses already noted that in addition to NMD activity on aberrant transcripts, the pathway participates in the decay of regular, physiological mRNAs as well (*4*). Most of the initially identified NMD-activating features on endogenous transcripts are in line with the above rules for PTC definition. For example, NMD is triggered by introns in 3' untranslated regions (UTRs), translated upstream open reading frames (uORFs) in 5' UTRs, or selenocysteine codons that are interpreted as stop codons. Later studies further showed that long 3' UTRs can activate NMD *per se*, in the absence of a downstream splice junction (*5, 6*). The generality of a “3' UTR length rule” has, however, been questioned recently in a nanopore sequencing-based study that (after removing the transcripts from the analysis for which there was evidence for splicing in the 3' UTR) found no predictive value of 3' UTR length for NMD regulation (*7*). Independently of which mechanisms trigger NMD on non-classical NMD substrates, it has been proposed that the expression of up to 20-40% of genes is directly or indirectly affected when NMD is inactivated in mammalian cell lines (*3, 7*), and it is tempting to speculate that the pathway may thus have extensive functions in physiological gene expression control (*1*). Most mammalian studies so far have used cell culture models, and it is therefore largely unknown whether the regulatory potential of NMD extends to the intact organ and living organism *in vivo*, and if so, which specific molecular and physiological pathways it controls.

Certain physiological processes are particularly reliant on rapid, well-controlled RNA turnover. Co-opting NMD could thus be especially opportune. In this respect, the circadian clock stands out as an important functional system that controls daily rhythms in transcription, mRNA and protein abundances, affecting thousands of genes across the organism and controlling daily changes in behaviour, physiology and metabolism (reviewed in (*8*)). In the mammalian body, the circadian system is hierarchically organised with a master clock in the brain's suprachiasmatic nucleus (SCN) that synchronizes peripheral clocks that operate in most cell types and that are responsible for driving cellular rhythmic gene expression programs. Across cell types, clocks have a similar molecular architecture, with a core clock mechanism that generates gene expression oscillations through transcription factors that interact in negative feedback loops. In the main loop, BMAL1:CLOCK (and/or BMAL1:NPAS2 in some neurons) function as the main activators and bind to E-box enhancers in their target genes, which include the *Period* (*Per1, 2*, *3*) and *Cryptochrome* (*Cry1, 2*) genes. Negative feedback is achieved when PER:CRY complexes repress their own transcription by inhibiting BMAL1:CLOCK. PER and CRY protein degradation temporally limits the repressive activity, eventually allowing a new cycle to ensue. Conceivably, rapid mRNA decay is critical for this mechanism as well (*9*) - as a means of restricting protein biosynthesis and availability in time - yet the responsible decay pathways remain overall poorly understood. Additional feedback mechanisms (in particular involving nuclear receptors of the REV-ERB/ROR families) interlock with the above main feedback loop and confer robustness to the system (reviewed in (*10*)). Via the rhythmic transcription factors generated through this clockwork, rhythmic mRNA production is driven at hundreds to thousands of clock-controlled genes (CCGs). The stability of CCG transcripts critically determines to what extent their initial transcriptional rhythms are propagated to the mRNA and protein abundance levels (*9*). Mechanisms that have been implicated in post-transcriptionally regulating rhythmic mRNAs in mammals include miRNA-mediated regulation (*11*) and regulated deadenylation (*12*). With regard to a possible involvement of NMD, evidence for roles in the circadian system has been reported from fungi, plants and flies (*13*-*16*). In mammals, the involvement of NMD in eliminating erroneous, rhythmic alternative splicing products is documented (*17*). How NMD globally shapes rhythmic transcriptomes, let alone in a mammalian organism *in vivo*, is still unknown.

In this study, we used a novel conditional NMD loss-of-function mouse model to uncover that NMD is directly implicated in regulating peripheral circadian clocks, rhythmic gene expression and food entrainment of the liver oscillator. We identify *Cry2* as a direct NMD target and further determine how the hepatic diurnal transcriptome is rewired in the absence of a functional NMD pathway. Our new mouse model and findings on circadian regulation provide important conceptual advances on *in vivo* functions of NMD and reveal a novel mechanism of post-transcriptional gene expression regulation that acts in the mammalian core clock.

Results

A novel conditional NMD loss-of-function allele based on SMG6 mutated in its nuclease domain

To inactivate NMD *in vivo* we generated mice in which we could conditionally recombine *Smg6*^{flox} to *Smg6*^{mut} (**Fig. 1A**), i.e. from an allele encoding wild-type SMG6 protein to a version specifically point-mutated at two of the three highly conserved aspartic acid (D) residues of the catalytic triade of the protein's PIN (PilT N-terminus) nuclease domain (*18*) (**Fig. 1B**). Briefly, we chose this strategy over a full gene knockout because NMD factors, including SMG6, carry additional functions in telomere and genome stability (*19*). These functions have been shown to be selectively maintained by expressing an NMD-inactive SMG6 protein lacking its nuclease domain (*20*). We first validated our genetic model in primary tail fibroblasts from homozygous *Smg6*$^{flox/flox}$ and *Smg6*$^{+/+}$ littermate mice that we stably transduced with a retroviral vector expressing tamoxifen-activatable CreERT2 (**Fig. 1C**). *Smg6*$^{flox/flox}$ cells specifically and efficiently recombined to *Smg6*$^{mut/mut}$ by addition of 4-hydroxytamoxifen (4-OHT) to the culture medium (**Fig. 1D**). In these cells, a lentiviral luciferase reporter carrying an intron in its 3' UTR became upregulated, as expected for an inactive NMD pathway (**Fig. 1E**). We further validated our model by RNA-seq to analyse gene expression changes transcriptome-wide in 4-OHT-treated and -untreated cells of both genotypes. Our method, based on random priming of rRNA-depleted total RNA, allowed for the quantification of both mRNA (exon-mapping reads) and pre-mRNA abundances (intron-mapping reads), the latter serving as a proxy for gene transcription rates (*11, 21, 22*). In analogy to previous studies (*11, 21*) we used mRNA/pre-mRNA ratios to estimate mRNA stability changes between NMD-inactive and control cells, and to distinguish them from secondary effects involving altered transcription rates. Our analyses revealed a shift to higher mRNA/pre-mRNA ratios (more stable mRNAs) specifically in NMD-inactive (*Smg6*$^{flox/flox}$ + 4-OHT) cells (**Fig. 2A**). Two transcript groups were particularly affected, (i) genes with known, annotated NMD-sensitive mRNA isoforms (according to Ensembl annotations) and (ii) genes with retained introns (**Fig. 2B**). Inspection of individual examples further validated these findings, as shown for *Hnrnpl* and *Srsf11*, with a clear up-regulation of NMD isoform-specific exons in the mutants (**Fig. 2C, D**). Transcriptome-wide differential expression analysis at the exon level pointed at hundreds of constitutive exons from canonical mRNAs (i.e., without annotated NMD isoforms) with increased abundance under *Smg6* mutant conditions, indicating widespread NMD regulation of the transcriptome (**Fig. 2E**).

We proceeded to analyse if specific transcript features correlated with *Smg6* mutation-dependent changes in mRNA/pre-mRNA ratios. As expected for potential NMD substrates, the transcripts that were most strongly affected were low expressed in control cells (**Fig. 2F**).

5' UTR length (which correlates with uORF content (*23*)) was weakly, though significantly, associated with increased mRNA/pre-mRNA ratios (**Fig. 2G**), suggesting that translated uORFs may contribute as an NMD-activating feature to endogenous mRNA upregulation in *Smg6* mutants. Stronger correlations were observed with the lengths of the CDS (**Fig. 2H**) and 3' UTRs (**Fig. 2I**). The latter association is consistent with the model that long 3' UTRs can function as NMD-activating features. Altogether, these associations matched those observed for other NMD loss-of-function models, e.g. in HeLa cells subjected to *Upf1* knockdown (*24*). Taken together, we concluded that our genetic model based on the mutant *Smg6* allele was suitable to analyse endogenous targets and functions of the NMD pathway.

NMD inactivation lengthens free-running circadian periods in fibroblasts and in liver

We next investigated how mutant *Smg6* affected the circadian clock. First, we stably transfected the above fibroblasts with a circadian reporter gene, *Dbp-Luciferase* (*25*), and recorded their free-running circadian rhythms upon NMD inactivation with 4-OHT. Briefly, we synchronised the cellular oscillators using temperature cycles (*26*), released them at 37°C, and continued real-time bioluminescence recordings for an additional 5 days under constant conditions (**Fig. 3A**). These experiments revealed a lengthening of the free-running circadian period in NMD-deficient cells by ca. 1.5 hours (**Fig. 3B**).

We next wished to corroborate a potential period phenotype using the liver as a peripheral clock model with direct links to circadian physiology and functions *in vivo*. We thus crossed into the *Smg6*^{flox} mouse line a hepatocyte-specific *CreERT2* (tamoxifen-activatable Cre, driven from the *Albumin* locus (*27*)) and a circadian reporter, *mPer2::Luc* (*28*). After intraperitoneal tamoxifen injections into young adult mice, animals were sacrificed 4 weeks later, a time at which highly efficient recombination of *Smg6*^{flox} to *Smg6*^{mut} had taken place (**Fig. 3H**). We then prepared organotypic slices (tissue explants) for real-time recording of luciferase rhythms *ex vivo* (**Fig. 3C**). In these experiments, we observed a strong and specific period lengthening by almost 3 hours in liver explants from animals with inactivated NMD (tamoxifen-treated *Smg6*$^{flox/flox}$ mice) as compared to livers from identically treated littermate animals of the control genotype (**Fig. 3D**). As a specificity control, we also recorded kidney explant rhythms from the same animals. Free-running periods were generally longer in this organ, as reported previously (*28*), yet we did not observe any differences between genotypes (**Fig. 3D**), in line with the hepatocyte-specific expression of CreERT2.

In vivo, and according to oscillator theory (*29, 30*), a difference in period lengths between the entraining clock (here: wild-type period SCN) and the entrained clock (here: long period *Smg6* mutant hepatocytes) will typically translate to a phase shift of the entrained oscillator. Thus, we expected that the long period mPER2::LUC rhythms seen in liver explants *ex vivo* would lead to a change in phase *in vivo*. To evaluate this prediction, we used a method for the real-

time recording of daily liver gene expression in freely moving mice (*31, 32*) that relies on luciferase reporters, luciferin delivery via an osmotic minipump, and highly sensitive bioluminescence photon counting (**Fig. 3E**). Using the same *mPer2::Luc* reporter knock-in animals (NMD-deficient vs. controls), real-time recording was carried out under conditions that ensured light-entrainment of the SCN clock to an external 24-hour light-dark cycle by means of a skeleton photoperiod, i.e. two 30 min light pulses applied at times corresponding to the beginning and to the end of the light phase in a 12h-light-12h-dark (LD12:12) cycle. We observed high-amplitude rhythmic bioluminescence rhythms in both genotypes (**Fig. 3F**). Intriguingly, the entrained phases of mPER2::LUC reporter oscillations were indistinguishable (**Fig. 3G**). Moreover, we next investigated the effect of the *Smg6* mutation on the central clock in the SCN. We stereotactically injected an adeno-associated virus (AAV) expressing *Cre::eGFP* to induce recombination (**Fig. S1A, B**) and scored circadian clock parameters by two different assays: (i) *in vivo*, we measured behavioural locomotor rhythms under constant conditions (free-running clock) by running wheel assays (**Fig. S1B, C**) and (ii) *ex vivo*, we recorded mPER2::LUC rhythms from SCN explants (**Fig. S1D-F**). Neither assay revealed an effect of the *Smg6* mutation on free-running periods for the SCN clock; yet, as a caveat, we also noted overall less efficient recombination as compared to our liver experiments (**Fig. S1G**). We concluded that loss of NMD triggered by the *Smg6* mutant allele had a strong period lengthening phenotype for peripheral clocks, notably for liver explants, that was, however, masked in the entrained liver of the intact animal when using mPER2::LUC as a readout.

NMD inactivation differentially affects the phases of core clock gene expression in the entrained liver

We next analysed the apparent discrepancy between the long periods of liver rhythms *ex vivo* (**Fig. 3C, D**) and the lack of a phase phenotype *in vivo* (**Fig. 3F, G**). Briefly, other tissues than liver (e.g. kidney (*33*)) may have contributed to the overall bioluminescence signal detected in the *in vivo* recording experiments, thereby masking a hepatic phase phenotype. Moreover, systemic cues that are dependent on the SCN, yet do not require a functional hepatocyte clock, can drive rhythmic PER2 accumulation in liver (*34, 35*); therefore, mPER2::LUC signal may not be representative of the intrinsic liver clock phase. In order to evaluate in a comprehensive fashion how rhythmic gene expression was altered *in vivo*, we collected livers at 4-hour intervals around-the-clock from LD12:12-entrained *Smg6* mutant and control mice, with timepoints ZT0 (*Zeitgeber* Time 0, corresponding to time of “lights-on”), ZT4, ZT8, ZT12 (“lights-off”), ZT16 and ZT20 (**Fig. 4A**). We carried out RNA-seq on all individual mouse liver samples (triplicates per genotype and timepoint) and assembled the data into two time series representing the diurnal liver transcriptome under conditions of an inactive vs. active NMD pathway. As a means of quality control, we first validated that known NMD targets were

upregulated in *Smg6* mutant livers. Indeed, as in the fibroblasts (**Fig. 2C, D**), NMD-annotated isoform exons were increased in abundance (**Fig. S2A**). Other transcripts diagnostic of an inactive NMD pathway showed the expected post-transcriptional upregulation as well. For example, mRNAs encoding components of the NMD machinery itself were post-transcriptionally upregulated (**Fig. S2B**), as reported previously from cell lines (*6*). This phenomenon has been proposed to represent an autoregulatory mechanism that involves as NMD-activating features the long 3' UTRs that these mRNAs carry. Similarly, the uORF-regulated *Atf4* and *Atf5* transcripts, which are documented NMD substrates (*4, 36*) and encode key transcription factors in the integrated stress response (ISR) (*37*), showed the expected upregulation (**Fig. S2C**). Of note, higher ATF5 protein accumulation (**Fig. S2D**, **E**) occurred in the absence of general ISR activation (as judged by eIF2α phosphorylation levels that were only weakly affected; **Fig. S2D**), pinpointing the lack of direct NMD regulation rather than proteotoxic stress as the likely trigger.

We then analysed the daily dynamics of core clock gene expression at the mRNA and pre-mRNA levels (**Fig. 4B-J**). Consistent with the *in vivo* recording of *mPer2::Luc* animals, *Per2* mRNA and pre-mRNA rhythms were highly similar between the two genotypes (**Fig. 4E**). By contrast, several other core clock genes - notably those encoding the main transcriptional activators, *Clock* and *Arntl/Bmal1* (**Fig. 4B, C**), as well as *Cry1* (**Fig. 4F**) and *Rorc* (**Fig. 4J**) - showed phase-delayed pre-mRNAs indicative of transcription occurring several hours later. The complete analysis of core clock mRNA (**Fig. 4K**) and pre-mRNA (**Fig. 4L**) rhythms revealed that the considerable phase differences seen for many core clock genes at the transcriptional (pre-mRNA) level (**Fig. 4L**), only partially propagated to the mRNA level (**Fig. 4K**). Of the core loop constituents, *Cry2* mRNA showed a substantial delay by ca. 2 hours (**Fig. 4G, K**). This later mRNA phase did not appear to originate from delayed transcription, given that the pre-mRNA phase of *Cry2* was, if anything, advanced (**Fig. 4G, L**). Other delays in mRNA accumulation that we observed affected the two nuclear receptors and components of the stabilizing loop, *Nr1d2/Rev-erbb* and *Rorc* (**Fig. 4H, J, K**).

NMD regulation of *Cry2* mRNA occurs through its 3' UTR and limits CRY2 protein accumulation during the dark phase

Among the core clock genes, the observed change in the daily *Cry2* expression profile (i.e., a peak in *Cry2* mRNA levels at ZT8-12 with subsequent decrease in control animals; yet *Cry2* mRNA abundance persisting on a high plateau until ZT20 in *Smg6* mutants; **Fig. 4G**) was consistent with the hypothesis that the *Cry2* transcript became stabilised in the absence of NMD. Indeed, the analysis of *Cry2* mRNA/pre-mRNA ratios across all liver samples suggested elevated stability during the dark phase of the cycle (ZT12-20) (**Fig. 5A**). Western blot analysis of total liver proteins revealed that the prolonged mRNA abundance under NMD-inactive

conditions led to corresponding changes at the level of CRY2 protein, whose peak accumulation was delayed by 4 hours in *Smg6* mutant animals (peak at ZT20) compared to controls (peak at ZT16) (**Fig. 5B, C**). Moreover, the analysis of individual livers showed that CRY2 reproducibly accumulated to >2x higher levels in *Smg6* mutant livers towards the end of the dark phase, at ZT20 (**Fig. 5D, E**). Furthermore, increased CRY2 levels were also apparent in *Smg6* mutant fibroblasts (**Fig. 5F, G**). These observations were compatible with a direct regulation of *Cry2* mRNA stability through NMD. To explore this hypothesis, we analysed whether the *Cry2* mRNA contained any potential NMD-activating features. First, we inspected RNA-seq coverage on the *Cry2* locus in our fibroblast data, which revealed the expression of a single *Cry2* transcript isoform carrying a long 3' UTR of ~2.2 kb (**Fig. 5H**; identical observations were made in the liver RNA-seq data from (*11*)), i.e. well beyond the ~1 kb cut-off that has been used as a benchmark for the definition of potential endogenous NMD substrates (*1, 5, 6*). There was no evidence that a second annotated mRNA isoform with a shorter 3' UTR (~0.4 kb; **Fig. 5H**) or any other, additional transcript variants were generated from the locus. Finally, with a 5' UTR that is particularly short (20 nt) and no evidence for translating ribosomes upstream of the annotated start codon according to previous ribosome profiling data (*23*), we excluded the possibility that the transcript contained NMD-activating uORFs. We thus assessed whether the ~2.2 kb *Cry2* 3' UTR would confer NMD regulation to a luciferase reporter gene (**Fig. 5I**). Dual luciferase assays revealed that inactivating NMD in fibroblasts led to a >5-fold activity increase for the *Cry2* 3' UTR-carrying reporter as compared to the control reporter (**Fig. 5J**), providing evidence that the *Cry2* 3' UTR can trigger NMD.

We wished to further validate NMD regulation of the *Cry2* 3' UTR by an approach that would allow more rapid and direct readout of reporter activity after NMD inhibition, rather than having to rely on prolonged 4-OHT treatment of reporter-expressing cells to induce the *Smg6* mutation. To this end, we used a pharmacological inhibitor of the kinase SMG1, hSMG-1 inhibitor 11e (SMG1i in the following) (*38*). Briefly, for this compound an IC_{50} in the sub-nanomolar range had originally been reported (*38*), yet subsequent studies *in vitro* (*39*) and in cells (e.g. (*40*)) have applied SMG1i at considerable higher concentrations (0.2-1 µM) to inhibit NMD; additional effects on other kinases (e.g. mechanistic target of rapamycin, mTOR (*38*)) cannot be excluded under these conditions. We observed a very strong effect of 0.6 µM SMG1i on circadian period in two commonly used circadian model cell lines, murine NIH/3t3 fibroblasts (**Fig. 6A, B**) and human U-2 OS osteosarcoma cells (**Fig. S3A, B**). Of note, the period lengthening phenotype caused by the compound (~4 hours; **Fig. 6B**) was considerably stronger than that seen in the genetic *Smg6* fibroblast model (~1.5 hours; **Fig. 3B**), in line with possibly broader activity of SMG1i. Moreover, cellular toxicity was observable after prolonged SMG1i treatment for several days. We thus concluded that this compound would be most appropriate for short-term NMD inhibition up to 24 hours, which is also the timeframe in which

it increased endogenous CRY2 protein abundance (**Fig. 6C**). We subsequently assessed how acute SMG1i treatment affected the activity of lentivirally delivered luciferase reporters carrying various core clock gene 3' UTRs, using real-time bioluminescence recording in mouse fibroblasts. Upon addition of SMG1i, output from a reporter carrying the *Cry2* 3' UTR increased rapidly within a few hours (**Fig. 6D**). By contrast, neither the vector 3' UTR, nor the 3' UTRs of other core clock genes that were similar in length to the *Cry2* 3' UTR, namely that of *Per1* (~1 kb) and *Per2* (~2.1 kb), showed increased reporter output. Based on this outcome, we concluded that the *Cry2* 3' UTR acted as a specific trigger of the NMD pathway. We next reasoned that the *Cry2* 3' UTR may be NMD-activating due to its length or, alternatively, that it could contain specific *cis*-acting elements important for NMD activity, e.g. specific binding sites for RNA binding proteins (RBPs). To distinguish between these two scenarios, we tested individual, overlapping fragments of the full-length *Cry2* 3' UTR in the reporter assay. In contrast to full-length *Cry2* 3' UTR, none of the fragments was associated with reporter upregulation upon SMG1i treatment (**Fig. 6E**). We concluded that most likely the considerable length of the *Cry2* 3' UTR was a feature that could trigger NMD.

With NMD downregulation leading, on the one hand, to longer periods and, on the other hand, to altered abundance and accumulation dynamics of CRY2, we next attempted to investigate whether there was a causal link between both effects. To this end, we produced *Cry2*-deficient NIH/3t3 cells (**Fig. 6F**) that we treated with SMG1i, based on the reasoning that NMD inhibition may have a less severe period phenotype in the absence of a functional *Cry2* gene. However, in this setup we did not uncover an evident modulation of SMG1i-mediated period lengthening by the absence of *Cry2* (**Fig. 6G**). A similar outcome was obtained in *Cry2*-deficient U-2 OS cells (**Fig. S3C, D**). We concluded that SMG1i was able to provoke period lengthening independently of *Cry2*. However, given the questions surrounding the specificity of SMG1i detailed above, an interaction of the period phenotype with *Cry2* regulation may have been masked by other, stronger effects of the compound. In the future, how NMD-mediated regulation of *Cry2* participates in period lengthening should be examined through dedicated experiments in $Smg6^{mut}$ cells/livers.

Transcriptome-wide analyses uncover rhythmic gene expression reprogramming in the entrained liver

We next analysed how the global rhythmic transcriptome was affected in *Smg6* mutant livers *in vivo*. Changes in gene expression in the mutant are likely a consequence of direct and indirect effects, due to (i) NMD directly controlling the mRNA stability for some clock-controlled output genes, which would post-transcriptionally impact on their amplitudes and phases; (ii) the altered phase of *Cry2* and other core clock components (**Fig. 4K**) impacting on the transcriptional timing and dynamics at clock-controlled loci; and (iii) additional secondary

consequences that could be both transcriptional and post-transcriptional in nature, as a result of the above effects. We first investigated whether there were global changes in the populations of rhythmic transcripts between the two genotypes, analysing the RNA-seq datasets from the above cohort (**Fig. 4A**). Using established rhythmicity detection algorithms (MetaCycle R package (*41*)), we found that the majority of mRNAs classified as rhythmic in controls, were also rhythmic in the *Smg6* mutant livers (N=1257; **Fig. 7A**); visual inspection of the pre-mRNA heatmaps suggested that most of these rhythms were driven through rhythmic transcription. A lower number of transcripts passed the rhythmicity criteria of the detection algorithm in only one of the genotypes, with genes whose mRNAs were specified as rhythmic in controls but non-rhythmic in *Smg6* mutants (N=223; **Fig. 7B**) and vice versa (N=323; **Fig. 7C**). Inspection of the heatmaps, however, indicated that in many cases, the alleged lack of rhythmicity in one or the other genotype was most likely the result of lower/noisier expression levels rather than clear-cut loss of oscillations (a well-known phenomenon when comparing rhythmic gene expression datasets (*42*)). We thus first focused our analyses on the common mRNA rhythmic genes. Their peak phase distributions globally resembled each other in the two genotypes (**Fig. 7D**). A large group of mRNAs showed maximal abundance around ZT6-12, an interval that overlaps with the expected peak mRNA phase of direct BMAL1:CLOCK targets containing E-box enhancers (*43*); this cluster appeared phase-advanced in *Smg6* mutants. Moreover, several phases were underrepresented in mutants as compared to controls, such as the distinct group of transcripts with maximal abundance at the beginning of the light phase in controls (ZT0-2) that was absent in *Smg6* mutant livers (**Fig. 7D**). For a more quantitative analysis of these effects, we calculated transcript-specific phase differences, which indicated that mRNA phases in *Smg6* mutants globally followed those in controls, with advances and delays spread out across the day (**Fig. 7E**). Overall, more transcripts were phase advanced (691 genes) than delayed (566 genes) in *Smg6* mutant livers (**Fig. 7F**). This outcome was unexpected given that the expression profiles for core clock transcripts (**Fig. 4B-J**), and specifically the findings on *Cry2* (**Fig. 5, Fig. 6**), had rather pointed towards a *delay* of the entrained liver clock in *Smg6* mutants. We then overlaid our rhythmic transcript set with data from a large circadian mouse liver ChIP-seq study (*22*). We observed that mRNAs arising from loci with binding sites for BMAL1 and CLOCK (**Fig. 7G**; 59/71 transcripts advanced/delayed; p=0.0065) or PER and CRY proteins (**Fig. 7H**; 73/76 advanced/delayed; p=0.0005) were indeed significantly skewed towards phase delays, in comparison to rhythmic genes that were not direct targets of these core clock proteins (**Fig. 7I**; 335/252 advanced/delayed; p=0.18). We concluded that multiple factors engendered complex phase changes at the rhythmic transcriptome level in *Smg6* mutants, manifesting in delays for many direct BMAL1:CLOCK targets, and overall advanced phases for many other rhythmically expressed mRNAs.

Next, we compared peak-to-trough amplitudes between the genotypes. For rhythmic mRNAs that are direct targets of NMD, increased transcript stability in *Smg6* mutants should lead to flattening of peak-to-trough ratios. To explore this possibility, we used the Z-scores (**Fig. 7A**) for the common rhythmic transcripts to calculate the amplitudes (maximum-to-minimum fold-changes) for mRNAs and for pre-mRNAs, which we compared between the two genotypes. In *Smg6* mutants, median mRNA amplitudes were lower than in controls, but pre-mRNA amplitudes were higher (**Fig. 7J**); when normalizing mRNA amplitudes for pre-mRNA fold-changes – as a means to control for differences in transcriptional rhythmicity at the locus – the decrease in rhythmic amplitudes in *Smg6* mutants was highly significant (**Fig. 7K**). This observation indicated that higher stability of rhythmic mRNAs in *Smg6* mutants was detectable at the global level. In the extreme case, an mRNA that is rhythmic in control animals may lose its amplitude to the extent that it would not anymore be considered as rhythmic at all; it would then group within the N=223 genes shown in **Fig. 7B**. We inspected the individual expression profiles of these genes, which led to the identification of a sizeable number of transcripts that displayed severely blunted mRNA amplitudes in *Smg6* mutants, despite similar rhythmic pre-mRNAs (i.e. oscillations in transcription) (**Fig. 7L**). For some of the cases, plausible hypotheses about underlying NMD-eliciµting features can be made. For example, according to our previous mouse liver ribosome profiling data (*23*), *Glycine decarboxylase (Gldc)* contains efficiently translated uORFs according to data from (*44*); in the case of *Lactate dehydrogenase B (Ldhb)*, a regulatory mechanism entailing stop codon readthrough has been demonstrated (*45*) and could provide a link between *Ldhb* translation and NMD. For the other transcripts shown in **Fig. 7L** (*Pde9a, Kyat1, Tubb4b, Tmem101, Amdhd1, Epha2*), no obvious candidate NMD-eliciting features are apparent.

Altered food entrainment of the liver clock in *Smg6* mutant animals

The above analyses demonstrated that the stably entrained liver clock, under *ad libitum* feeding and LD12:12 conditions, was subject to phase and amplitude alterations at the level of clock-controlled gene expression. Our *in vivo* recording experiments (**Fig. 3E-G**) had been insensitive to picking up such differences in liver rhythms due to the use of the *mPer2::Luc* reporter allele, whose phase was unaffected by *Smg6* mutation under stable entrainment conditions. We reasoned that under conditions where the stable entrainment was challenged, a phenotype may be unmasked also for *mPer2::Luc*. To this end, we carried out food shifting experiments i.e., switching from *ad libitum* to daytime feeding. Under these conditions, the liver clock receives conflicting timing cues from the SCN and from feeding/fasting cycles (**Fig. 8A**), which are not anymore aligned to each other and will eventually lead to an inversion of hepatic oscillator phase due to the dominance of feeding *Zeitgebers* for peripheral oscillators (*46*). The kinetics and endpoint of phase adaptation can be understood as a paradigm of clock

plasticity/rigidity and can be recorded using the RT-Biolumicorder setup (*32*). Our experiments revealed that in *Smg6* mutant animals, after 3 days of feeding during the light phase, daily cycles in bioluminescence had readjusted to a phase that substantially differed between control and *Smg6* mutant animals (3 hours difference at trough/0.5 hours at peak; **Fig. 8B, C**). We concluded that the NMD pathway is important for the adaptation of circadian gene expression to food entrainment in mouse liver, and for how distinct timing cues are integrated within the clock circuitry. Moreover, we noted that the activity traces (infrared beam break) recorded in the RT-Biolumicorder setup from the same animals (**Fig. 8D, E**) suggested genotype-dependent changes in locomotor activity patterns, i.e a typical output of the SCN clock. Previous findings have indicated that rhythmic liver metabolism can feedback to the brain and manifest in altered behaviour, notably involving liver-derived ketone bodies that impact food anticipatory behaviour (*47*). Our data could suggest that in the absence of a functional NMD pathway, such mechanisms may be altered as well.

Discussion

Our novel conditional *Smg6* endonuclease-mutant allele provides unique possibilities to explore *in vivo* activities of the NMD pathway and has allowed us to reveal an unexpected role within the mammalian circadian system – a conserved, key mechanism for the organisation of daily rhythms in behaviour, physiology and metabolism. We uncover that NMD loss-of-function has a striking impact on free-running circadian periods in two peripheral clock models, primary fibroblasts and liver, and on gene expression oscillations in stably entrained and food-shifted livers. Moreover, we identify a specific core clock component, *Cry2,* as NMD-regulated and attribute the NMD-eliciting activity to its long 3' UTR. Although it is widely accepted that efficient mRNA decay is critical for the establishment of gene expression oscillations (*9*), which specific pathways mediate the decay of transcripts encoding core clock components has remained largely unknown. It is intriguing that NMD has been co-opted for this purpose, and future work should address whether in the specific case of *Cry2* this mechanism offers regulatory advantages over other decay routes, or whether it simply reflects that nature and evolution are “opportunistic” in that they employ available molecular pathways in the most efficient fashion. In line with this idea is the observation that a sizeable number of other rhythmic transcripts appears to rely on NMD to ensure efficient mRNA turnover as well (**Fig. 7L**). More generally, it would be interesting to further explore the evolutionary pressures relating to NMD activity on physiological transcripts; for example, it has been speculated why many mammalian mRNAs contain long 3' UTRs but evade NMD, and a model has been put forward suggesting that such mRNAs have evolved to recruit NMD-inhibiting RBPs in spatial proximity of the termination codon (*5*). However, an opposite drive to attract and retain NMD regulation would be plausible as well – acting on endogenous transcripts, such as *Cry2*, whose

intrinsic instability is physiologically important. These ideas are in line with findings that in the circadian systems of *Neurospora* (*15, 16*), *Arabidopsis* (*13*) and *Drosophila* (*14*), roles for NMD have emerged as well.

In the absence of NMD, CRY2 protein in liver accumulates to higher levels and for an extended time. Based on the experiments presented in our study, we are not yet fully in the position to evaluate to what extent these effects are directly responsible for the period lengthening. Still, it would be plausible that the phase delay of CRY2 seen in the *Smg6* mutants could be critically involved. According to around-the-clock ChIP-seq data from wild-type mouse liver, CRY2 binds and represses its target genes at circadian time CT15-16 (*22*), thus closely matching the timing of maximal CRY2 abundance in our control mice (ZT16). The ChIP-seq data from wild-type livers further indicate that by CT20, CRY2 is cleared and replaced by CRY1, which binds to chromatin with a peak at around CT0 and is associated with a transcriptionally repressed, but poised state of BMAL1:CLOCK activity. Period lengthening through the prolonged availability of CRY2 may thus involve an extended CRY2-mediated repressive phase and/or CRY2 denying its homolog CRY1 access to its targets, causing a delay in the handover to CRY1. Of note, the period lengthening we observe is phenotypically comparable to that reported for a chemical, selective stabiliser of CRY2 protein, which also prolongs periods in reporter assays across several cell types and species (*48*). Moreover, period lengthening has also been reported upon CRY2 stabilisation (in a *Cry1*-deficient background) induced by genetic inactivation of the CRY-specific ubiquitin ligase *Fbxl3* (*49*). For these reasons – and reminiscent of findings on CRY1 accumulation (*50*) – the changed timing of CRY2 accumulation, rather than its generally higher levels, may be a critical feature for the period phenotype and for the phase effects seen in the entrained liver. We thus propose that *Cry2* mRNA instability, mediated through NMD, is an important mechanism within the core loop of the clock by which CRY2 protein biosynthesis is restricted to the beginning of the dark phase when it acts in sync with PER1 and PER2 to repress CLOCK:BMAL1-mediated transcription (**Fig. 9**). Concomitant with CRY2/PER1/PER2 some CRY1 is recruited, yet the majority is found to join CLOCK:BMAL1 after CRY2/PER1/PER2 removal (*22*), leading to the formation of the late repressive and poised states that precede the next transcriptional cycle at CLOCK:BMAL1-bound E-box enhancers.

The data we present suggest specificity of the phenotype for peripheral clocks. Indeed, we were unable to detect an impact on circadian period for the master clock in the SCN. Different explanations may underlie this observation. First, we cannot exclude lack of phenotype due to technical reasons, in particular a lower efficiency of Cre-mediated recombination in SCN neurons, or slower replacement kinetics of wild-type SMG6 by its mutant version due to different protein stability in neurons. For possible biological explanations, the decay of NMD

substrates may be less reliant on SMG6 in neuronal cells, or the strong intercellular coupling in the SCN (*51*) could render the clocks resilient to genetic perturbations of the NMD pathway. Finally, it has been reported that the relative importance of the two homologs, CRY1 and CRY2, in the negative feedback loop can be surprisingly tissue-specific. There is evidence that CRY1 rather than CRY2 is the main transcriptional repressor in the SCN (*49*), which could contribute to the insensitivity of the central clock to *Smg6* mutation.

An important difference between central and peripheral clocks lies in their response to food entrainment: liver and other peripheral clocks can be synchronised to feeding-fasting cycles in a way that can override entrainment signals from the SCN, while the SCN clock itself is generally not food-sensitive (*46, 52*). Comparing liver and SCN, it is intriguing that there is a correlation between the *Smg6*-dependent period phenotype (liver: long period; SCN: no period change) and the known ability to respond to food entrainment (liver: entrainable; SCN: not entrainable) and that in addition, the response to food entrainment is itself altered in *Smg6* mutant livers (**Fig. 8**). Different signalling pathways have been identified as mediators of food entrainment, notably feeding-regulated hormones such as insulin and insulin-like growth factor 1 (IGF-1) (*53*) and mTOR activation, which abundantly crosstalks with the circadian oscillator in liver (*53-57*). With mTOR acting as a master regulator of mRNA translation (*58*) and insulin/IGF-1-dependent clock entrainment involving miRNA-mediated regulation (*53*), a central role of RNA regulation in food entrainment is emerging, and it will be exciting to decipher how NMD further integrates into these mechanisms at the molecular level.

In summary, the unexpected role of NMD that we uncover within the circadian system illustrates the ongoing shift in perception of NMD from surveillance to housekeeping functions. We anticipate that our mouse model will provide valuable insights into so-far unidentified NMD targets and functions in mammals *in vivo*, including in the context of pathologies where NMD may represent a promising therapeutic target, such as in neurological diseases (*59*) and in cancer (*60*) .

Materials and Methods

Animals

All animal experiments were performed according to the cantonal guidelines of the Canton of Vaud, Switzerland, license VD3611. Healthy adult male mice of age 12-24 months were used. All mouse lines were maintained on a C57BL/6J background. The alleles *AlbCre-ERT2*^{ki} (*27*) and *mPer2::Luc*^{ki} (*28*) have been previously described. The novel *Smg6*^{flox} allele was generated in collaboration with Taconic (official nomenclature of line: *Smg6*$^{tm5498(D1352A,D1391A)Tac}$).

Primary fibroblasts and immortalisation

Adult male *Smg6*$^{flox/flox}$ and *Smg6*$^{+/+}$ control littermate mice were anaesthetised, euthanised and approximately 1 cm of tail tip was recovered and further sliced into thin pieces under sterile conditions. Tissue fragments were overnight digested with 1 mg/ml collagenase type 1A (Sigma Aldrich) in culture medium at 37°C. The culture medium consists of DMEM with 15% fetal calf serum (FCS), 1% Penicillin-Streptomycin-Glutamine (Thermo Fisher Scientific, 10378016), 1% non-essential amino acids (Thermo Fisher Scientific, 11140050), 1 mM sodium pyruvate (Thermo Fisher Scientific, 11360070), 87 mM β-mercaptoethanol, 18 mM HEPES pH 7.0 (Thermo Fisher Scientific, 15630080), 2.5 μg/ml Amphotericin B (Thermo Fisher Scientific, 15290018) and 2.5 μg/ml Plasmocin (InvivoGen).
Isolated fibroblasts became spontaneously immortal upon continuous culture, creating *Smg6*$^{flox/flox}$ or *Smg6*$^{+/+}$ cell lines. Immortalised fibroblasts were transduced with a retrovirus carrying a tamoxifen-inducible Cre and puromycin resistance (MSCV *CreERT2* puro, Addgene plasmid #22776). Retrovirus production was performed using the pCL-eco (Addgene, 12371) and pCMV-VSV-G (Addgene, 8454) plasmids in 293FT HEK cells using the CalPhos™ Mammalian Transfection Kit (Takara bio, 631312). Following 2 μM tamoxifen treatment, renewed every 24h for 4 consecutive days, the cells were utilised for experiments after 7-10 days.

DNA genotyping

DNA from cell cultures, liver or kidney was extracted using the DNeasy® Blood & Tissue Kit (Qiagen, 69504) according to the manufacturer's protocol. Genotyping PCR reaction was performed using HotStar Taq DNA polymerase (Qiagen, 203207), 0.4 mM primers (Microsynth), 0.2 mM dNTP mix (PROMEGA, U1511) and approximately 200-700 ng of DNA template. The primer sequences are as follows (5'-3'): Forward: gaa ata cca ggg ccc ttg c , Reverse1: cat cac tac cca gct cag gaa c, Reverse2: gga ttg gct cct ctt tgc tg. The PCR program is as follows : 15 sec at 95°C, 35 cycles : 1 min at 94°C, 1 min at 61°C, 1 min at 72°C and

final elongation at 72°C for 10 min. DNA extraction from dissected SCN tissue was done by Arcturus® PicoPure® DNA Extraction Kit (Thermo Fisher Scientific, KIT0103). PCR reaction was set up as above. The primer sequences are as follows (5'-3'): Forward gaa ata cca ggg ccc ttg c, Reverse2: tct agc tcc ttt ctg cct ctt c. The PCR program is as follows : 15 sec at 95°C, 40 cycles : 1 min at 94°C, 1 min at 55°C, 1 min at 72°C and final elongation at 72°C for 10 min.

Luciferase reporters and lentiviral production

CreERT2 Smg6$^{flox/flox}$ and *Smg6*$^{+/+}$ immortalised fibroblasts were transduced with a lentivirus carrying a dual luciferase (Firefly/Renilla) NMD reporter or a control vector. For the generation of dual luciferase reporter plasmids, the prLV1 dual luciferase reporter plasmid (*11*) was used, with or without the introduction of an intron downstream of the *Firefly* stop codon. For the latter, the chimeric intron of the pCI-neo vector (Promega, E1841) was cloned into the 3' UTR of the prLV1 vector. The following primers were used for PCR amplification: forward: aaagcggccGCTCGTTTAGTGAACCGTC (introducing a NotI restriction site) and reverse: tTTCTCGAGCTGTAATTGAACTGGGAG (introducing a XhoI restriction site). *Dbp-Luciferase* (*25*) and the 3' UTR luciferase reporters (*11*) have been described previously. Lentiviral particles were produced in 293FT cells using the envelope vector pMD2.G and the packaging plasmid psPAX2 as in previous studies (*11, 23*). Filtered viral supernatant was spun 2h at 24,000 rpm, 4°C using Optima L-90K Ultracentrifuge (SW32Ti rotor; Beckman), then viral particles were resuspended with normal growth medium and used for cell transduction.

Circadian bioluminescence recording of cell cultures

For mouse cell experiments, fibroblasts cultured in 35 mm culture dishes (Falcon) were synchronised either with serum shock (50% horse serum for 3h) or with temperature entrainment (cycles of 16h at 35°C and 8h at 37°C for 5 days). During recording cells were cultured in phenol-free DMEM (Gibco) containing 10% FBS, 1% PSG and 0.1 mM of luciferin, sealed with parafilm to avoid evaporation, in the LumiCycler setup (Actimetrics) at 37°C and 5% CO_2. NIH/3T3 murine fibroblasts were cultured under the same conditions as the immortalised fibroblasts but synchronised with 100 nM dexamethasone treatment for 15 min. SMG1 inhibitor (hSMG-1 inhibitor 11e; Probechem Cat. No. PC-35788) (*38*) was used as 10 mM stock (dissolved in DMSO) and, if not indicated otherwise, used at a concentration of 0.6 µM (NIH/3T3 experiments) to 1µM (*Smg6*^{flox} fibroblasts).

Dual luciferase assay

After lentiviral transduction cells were collected using 5x Passive Lysis Buffer (Promega) and luciferase activity was measured using the Dual-Glo Luciferase Assay System (Promega,

E1910) according to the manufacturer's protocol. *Firefly*-Luciferase signal was normalised to *Renilla*-Luciferase, and for each construct (3' UTR or NMD reporter) this signal was then normalised to that of lentivector-control plasmid (only containing generic vector 3′ UTR) treated with vehicle (for each experiment).

Experiments in human U-2 OS cells

U-2 OS (human, female, ATCC HTB-96) osteosarcoma cells harbouring a murine *Bmal1* promoter driven firefly luciferase reporter and derived *CRY2*-knock-out cell lines (clone D4) were described earlier (*61, 62*). *CRY1*-Luc and *CRY2*-Luc knock-in reporter cells were generated by introducing a luciferase ORF into the genomic locus 5' to the stop codon as described (*63*). For bioluminescence recording, cells were seeded into a 96 well plate in DMEM (Gibco #41965039), supplemented with 10% FBS, 25 mM HEPES, 1x PenStrep, at a density of 20.000 cells per well and grown for 3 days in an incubator at 37°C, 5% CO_2. Cells were synchronised by addition of 1 µM dexamethasone for 20 min. Medium was removed, wells were washed two times with prewarmed PBS, and luciferase activity was recorded at 35°C in phenol red-free DMEM (Gibco #21063029), supplemented with 10% FBS, 1x PenStrep, 250 µM D-Luciferin (PJK biotech, #102113), and inhibitor or vehicle control as indicated, using a TopCountNxt device (PerkinElmer) with a plate stacker.

RNA and library preparation

For fibroblast RNA-seq, cells of the various conditions ($Smg6^{+/+}$, $Smg6^{flox/flox}$; with/without 4-OHT) were cultured for at least 3-4 days after seeding, to allow desynchronisation of circadian oscillators; medium was removed, cells were lysed on the plate with TRI reagent (Sigma), and RNA extracted according to the manufacturer's protocol. RNA from snap-frozen liver pieces was extracted essentially as described (*11*). RNA-seq libraries were prepared from triplicates/condition for cell culture experiments or from individual mouse livers according to standard protocols (TruSeq® Stranded Total RNA Library Prep Gold, Illumina) using 1 µg starting material. Paired-end sequencing (150 bases) was carried out on Illumina HiSeq 4000 (fibroblasts) and NovaSeq 6000 (liver) platforms at the Lausanne Genomic Technologies Facility to a sequencing depth of at least 25 million (fibroblasts) and 100 million (liver) cDNA-mapping reads per sample. At these sequencing depths, previous studies (e.g. (*21*)) have shown that it is possible to reliably quantify several thousand genes at both intronic and exonic level, and that post-transcriptional regulation can be discerned from transcriptional changes.

RNA sequence analysis

Reads were mapped on the mouse genome GRCm38 (Ensembl version 91) using STAR (*64*) (v. 2.7.0f; options: --outFilterType BySJout --outFilterMultimapNmax 20 --

outMultimapperOrder Random --alignSJoverhangMin 8 --alignSJDBoverhangMin 1 --outFilterMismatchNmax 999 --alignIntronMin 20 --alignIntronMax 1000000 --alignMatesGapMax 1000000). Read counts in genes loci were evaluated with htseq-count (*65*) (v. 0.13.5) for transcript mapped reads (i.e. exons; options: --stranded=reverse --order=name --type=exon --idattr=gene_id --mode=intersection-strict) and for whole locus mapped reads (i.e. exons plus introns; options: --stranded=reverse --order=name --type=gene --idattr=gene_id --mode=union). Read counting for exon analysis was not possible with htseq-count (most reads spanned multiple exons and would have been discarded) so a new python script was developed for this task. To avoid counting reads spanning different exons multiple times, the script calculated average read depth for each exon. Read pileups for gene loci were calculated using samtools depth (*66*) (v. 1.9) and plotted using R (v 4.1.1). Differential expression analysis was done in R using DESeq2 package (*67*). We applied a cut-off of at least 10 reads in at least 3 samples in the liver datasets for a gene to be considered as quantifiable at both intron and exon level; a total of 14104 genes passed that limit. RNA stability estimates were performed using RPKM normalised reads counts. Phase analysis was performed using RPKM normalised reads counts and the MetaCycle R package (*41*).

Induction of liver-specific *Smg6* mutation

8-12 week-old male *Smg6*$^{flox/flox}$ mice, carrying the liver-specific *Albumin*-driven *CreERT2* (allele *Alb*$^{tm1(cre/ERT2)Mtz}$ (*27*)), and their control littermates (*Smg6*$^{+/+}$) received 4 intraperitoneal injections of 20 mg/ml tamoxifen (Sigma-Aldrich) in corn oil at a dosage of 75 mg tamoxifen/kg of body weight. The mice were admitted to experiments 4 weeks later.

Liver and kidney explants

Male *Smg6*$^{flox/flox}$ mice and their control littermates *Smg6*$^{+/+}$ were euthanised following anaesthesia by isoflurane inhalation. Liver and kidney tissue were excised and put immediately in ice-cold Hank's buffer (Thermo Fisher Scientific). The outermost edges of the tissues were carefully excised in a sterile cabinet, and immediately placed on 0.4 micron Millicell cell culture inserts (PICMORG50) placed in 35 mm dishes with phenol-free DMEM (Thermo Fisher Scientific, 11880028) containing 5% FBS, 2 mM glutamine, 100 U/ml penicillin, 100 µg/ml streptomycin and 0.1 mM luciferin. The parafilm-sealed plates were placed for recording in the LumiCycler (Actimetrics) at 37°C and 5% CO_2.

RT-Biolumicorder experiments

Adult male mice, 12-20 weeks of age, carrying the genetically encoded circadian reporter allele *mPer2::Luc* (*28*) were used for the RT-Biolumicorder experiments. The experimental procedure followed our recently published protocol (*31*). Briefly, Alzet mini-osmotic pumps

(model 100D5 or 2001) were filled with 90 mg/ml with D-Luciferin sodium salt, dissolved in Phosphate Buffered Saline (PBS, pH 7.4) under sterile conditions. The pumps were closed with blue-coloured flow moderators (ALZET) and activated at 37°C according to the manufacturer's instructions, followed by the subcutaneous, dorsal implantation. As analgesics, carprofen (rimadyl, 5 mg/kg subcutaneous), and paracetamol (2 mg/ml, via drinking water) were administered. Prior implantation the dorsal area of the mouse at the site where the liver is positioned was shaved using an electric razor. The RT-Biolumicorder (Lesa-Technology) consists of a cylindrical cage for a single mouse with photon-reflecting walls, equipped with a photomultiplier tube (PMT), water and food containers and a built-in infrared sensor that records locomotor activity (*31, 32*). The RT-Biolumicorder records photon and activity levels in 1 min intervals. The data, which also contains light and food access information, was saved as text files and later analysed using the MatLab-based "Osiris" software according to (*31*), or by a custom-made R script.

Running wheel experiments

12-16 week-old male mice were single-housed in cages equipped with a running wheel and were placed in a light-tight cabinet. After approximately 10 days of habituation in 12h-light-12h-dark the mice were released in constant darkness for approximately 14 days. For the running wheel experiments with SCN-specific *Smg6* mutant recombination, the same protocol was used, followed by 14 days of post-injection recovery under 12h-light-12h-dark conditions and a second period of constant darkness for 14 days (adapted from (*68*)).

SCN-specific *Smg6* mutant mice

Male adult $Smg6^{flox/flox}$ mice and their control littermates ($Smg6^{+/+}$) received bilateral stereotactic injections of CMV.HI-Cre::eGFP AAV5 particles (AddGene, 105545) into the SCN (400 nl per site). Stereotactic coordinates: AP= - 0.34 ML= +/- 0.4, V=5.5. Ketamine/Xylazine (80/12.5 mg/kg) by intraperitoneal injection was used as anaesthetic and 5 mg/kg carprofen was administered subcutaneously for analgesia. Additionally, paracetamol (2 mg/ml) was administered via drinking water 1 day prior and 3 days following the procedure. Animal recovery was monitored for ten days. Mice carrying *mPer2::Luc* (*28*) in addition to $Smg6^{flox/flox}$ (experimental) or $Smg6^{+/+}$ (control) were used for the bioluminescence recording of SCN slices. For evaluation of viral targeting, mice were transcardially perfused with phosphate-buffered saline (PBS) followed by 4% paraformaldehyde (PFA). Brains were post fixed overnight in 4% PFA at 4°C and then cryopreserved in 30% sucrose solution in PBS for at least 24 hours at 4°C (until completely sunk to the bottom of the container). Cryopreserved brains were frozen and sliced in 25 µm thick sections. Sections were mounted using DAPI-fluoromount. Fluorescent images were acquired on a ZEISS Axio Imager.M2 microscope,

equipped with ApoTome.2 and a Camera Axiocam 702 mono. Specific filter sets were used for the visualisation of green (Filter set 38 HE eGFP shift free [E] EX BP 470/40, BS FT 495, EM BP 525/50) and blue (Filter set 49 DAPI shift free [E] EX G 365, BS FT 395, EM BP 445/50) fluorescence. For genomic DNA extraction, fresh brain tissue was collected in RNA*later* solution (Invitrogen) and kept at 4°C for 2 weeks. Then 250 µm thick sections containing the SCN were sliced using a microtome and the SCN region was microdissected under a fluorescent equipped stereomicroscope (Nikon SMZ-25).

SCN slices and bioluminescence recording

Following bilateral stereotactic injections as described in the previous paragraph, approximately 14 days later the mice were sacrificed and the SCN was dissected. Slices of 350 µm around the area of the SCN were prepared with a tissue chopper between ZT4.8 and ZT6.3; 2 slices per animal were used. Slicing and recovery buffer consisted of NMDG aCSF (85 mM NMDG, 9 mM $MgSO_4$, 2.3 mM KCl, 1.1 mM NaH_2PO_4, 0.5 mM $CaCl_2$, 23 mM D-Glucose, 28 mM $NaHCO_3$, 18 mM Hepes, 3 mM Na-pyruvate, 5 mM Na-ascorbate and 2 mM thiourea; pH 7.3-7.4; 300-310 mOsm/kg according to (*69*)). Each slice was cultured in a single well of a 24-well plate in 300 µl of culture medium (0.7 x MEM Eagle medium with 1.7 mM $MgSO_4$, 0.8 mM $CaCl_2$, 11 mM D-Glucose, 17 mM $NaHCO_3$, 25 mM Hepes, 0.4 mM GlutaMAX, 17% Horse serum, 0.8 mg/L Insulin, 0.8495 mM Ascorbic acid, 1% penicillin/streptomycin and 100 µM Luciferin; pH 7.3-7.4; 300-310 mOsm/kg according to (*69*)). Viral transduction and accurate injection localisation of the SCN was evaluated with fluorescent imaging with THUNDER Imaging Systems widefield microscope (Leica) on the 8th day in culture. Circadian bioluminescence was monitored using photomultiplier tubes (PMTs) for approximately one week at 34.5 °C with 5% CO_2 (in-house built device).

Protein extraction and Western Blot

Total proteins from mouse liver samples were extracted in principle according to the NUN procedure (*70*): livers were homogenised in 2 tissue volumes of 10 mM Hepes pH 7.6, 100 mM KCl, 0.1 mM EDTA, 10% Glycerol, 0.15 mM spermine, 0.5 mM spermidine for 20 seconds using a Teflon homogenizer. 4 tissue volumes of 2x NUN Buffer (2 M Urea, 2% NP40, 0.6 M NaCl, 50 mM Hepes pH 7.6, 2 mM DTT, 0.1 mM PMSF; supplemented with complete protease inhibitor tablets, Roche) were added dropwise, on a vortex with constant low speed to ensure immediate mixing. Lysates were incubated 30 min on ice and cleared through centrifugation at 10000 rpm, 4°C, for 20 min. Supernatants were stored at -80°C. Aliquots of the lysates (20-30 µg of protein loaded per lane, either from a pool from 3 mice or from individual mice, as indicated) were separated by SDS-PAGE and transferred to PVDF membrane using iBlot 2 gel transfer device. After blocking (5% milk in TBST; 1 hour at room temperature), the

membrane was incubated overnight at 4°C with appropriate dilutions of primary antibodies, including anti-CRY2 (kind gift from Ueli Schibler, Geneva), anti-ATF5 (Abcam-ab184923), and anti-HSP90 (Cell signaling-4874), p-eif2alpha (Cell signaling-9721), eif2alpha (Cell signaling-9722). Following TBST washing (3 x 5 minutes), the membranes were incubated with the appropriate secondary antibody conjugated with HRP for 60 minutes at room temperature, followed by washing as above. Chemiluminescence signal was detected with Supersignal West Femto Maximum Sensitivity Substrate (Thermo Fisher Scientific, 34095), as described by the manufacturer. The quantification of bands was performed using ImageJ software.

References

1. T. Kurosaki, M. W. Popp, L. E. Maquat, Quality and quantity control of gene expression by nonsense-mediated mRNA decay. *Nature reviews. Molecular cell biology* **20**, 406-420 (2019).
2. M. Huth, L. Santini, E. Galimberti, J. Ramesmayer, F. Titz-Teixeira, R. Sehlke, M. Oberhuemer, S. Stummer, V. Herzog, M. Garmhausen, M. Romeike, A. Chugunova, F. Leesch, L. Holcik, K. Weipoltshammer, A. Lackner, C. Schoefer, A. von Haeseler, C. Buecker, A. Pauli, S. L. Ameres, A. Smith, A. Beyer, M. Leeb, NMD is required for timely cell fate transitions by fine-tuning gene expression and regulating translation. *Genes & development* **36**, 348-367 (2022).
3. V. Boehm, S. Kueckelmann, J. V. Gerbracht, S. Kallabis, T. Britto-Borges, J. Altmuller, M. Kruger, C. Dieterich, N. H. Gehring, SMG5-SMG7 authorize nonsense-mediated mRNA decay by enabling SMG6 endonucleolytic activity. *Nature communications* **12**, 3965 (2021).
4. J. T. Mendell, N. A. Sharifi, J. L. Meyers, F. Martinez-Murillo, H. C. Dietz, Nonsense surveillance regulates expression of diverse classes of mammalian transcripts and mutes genomic noise. *Nature genetics* **36**, 1073-1078 (2004).
5. G. Singh, I. Rebbapragada, J. Lykke-Andersen, A competition between stimulators and antagonists of Upf complex recruitment governs human nonsense-mediated mRNA decay. *PLoS biology* **6**, e111 (2008).
6. H. Yepiskoposyan, F. Aeschimann, D. Nilsson, M. Okoniewski, O. Muhlemann, Autoregulation of the nonsense-mediated mRNA decay pathway in human cells. *Rna* **17**, 2108-2118 (2011).
7. E. D. Karousis, F. Gypas, M. Zavolan, O. Muhlemann, Nanopore sequencing reveals endogenous NMD-targeted isoforms in human cells. *Genome biology* **22**, 223 (2021).
8. K. H. Cox, J. S. Takahashi, Circadian clock genes and the transcriptional architecture of the clock mechanism. *Journal of molecular endocrinology* **63**, R93-R102 (2019).
9. G. Le Martelot, D. Canella, L. Symul, E. Migliavacca, F. Gilardi, R. Liechti, O. Martin, K. Harshman, M. Delorenzi, B. Desvergne, W. Herr, B. Deplancke, U. Schibler, J. Rougemont, N. Guex, N. Hernandez, F. Naef, X. C. Cycli, Genome-wide RNA polymerase II profiles and RNA accumulation reveal kinetics of transcription and associated epigenetic changes during diurnal cycles. *PLoS biology* **10**, e1001442 (2012).
10. C. L. Partch, C. B. Green, J. S. Takahashi, Molecular architecture of the mammalian circadian clock. *Trends in cell biology* **24**, 90-99 (2014).
11. N. H. Du, A. B. Arpat, M. De Matos, D. Gatfield, MicroRNAs shape circadian hepatic gene expression on a transcriptome-wide scale. *eLife* **3**, e02510 (2014).
12. S. Kojima, E. L. Sher-Chen, C. B. Green, Circadian control of mRNA polyadenylation dynamics regulates rhythmic protein expression. *Genes & development* **26**, 2724-2736 (2012).
13. Y. J. Kwon, M. J. Park, S. G. Kim, I. T. Baldwin, C. M. Park, Alternative splicing and nonsense-mediated decay of circadian clock genes under environmental stress conditions in Arabidopsis. *BMC Plant Biol* **14**, 136 (2014).

14. H. Ri, J. Lee, J. Y. Sonn, E. Yoo, C. Lim, J. Choe, Drosophila CrebB is a Substrate of the Nonsense-Mediated mRNA Decay Pathway that Sustains Circadian Behaviors. *Mol Cells* **42**, 301-312 (2019).
15. Y. Wu, Y. Zhang, Y. Sun, J. Yu, P. Wang, H. Ma, S. Chen, L. Ma, D. Zhang, Q. He, J. Guo, Up-Frameshift Protein UPF1 Regulates Neurospora crassa Circadian and Diurnal Growth Rhythms. *Genetics* **206**, 1881-1893 (2017).
16. C. M. Kelliher, R. Lambreghts, Q. Xiang, C. L. Baker, J. J. Loros, J. C. Dunlap, PRD-2 directly regulates casein kinase I and counteracts nonsense-mediated decay in the Neurospora circadian clock. *eLife* **9**, (2020).
17. A. Neumann, S. Meinke, G. Goldammer, M. Strauch, D. Schubert, B. Timmermann, F. Heyd, M. Preussner, Alternative splicing coupled mRNA decay shapes the temperature-dependent transcriptome. *EMBO Rep* **21**, e51369 (2020).
18. F. Glavan, I. Behm-Ansmant, E. Izaurralde, E. Conti, Structures of the PIN domains of SMG6 and SMG5 reveal a nuclease within the mRNA surveillance complex. *The EMBO journal* **25**, 5117-5125 (2006).
19. C. M. Azzalin, J. Lingner, The double life of UPF1 in RNA and DNA stability pathways. *Cell cycle* **5**, 1496-1498 (2006).
20. T. Li, Y. Shi, P. Wang, L. M. Guachalla, B. Sun, T. Joerss, Y. S. Chen, M. Groth, A. Krueger, M. Platzer, Y. G. Yang, K. L. Rudolph, Z. Q. Wang, Smg6/Est1 licenses embryonic stem cell differentiation via nonsense-mediated mRNA decay. *The EMBO journal* **34**, 1630-1647 (2015).
21. D. Gaidatzis, L. Burger, M. Florescu, M. B. Stadler, Analysis of intronic and exonic reads in RNA-seq data characterizes transcriptional and post-transcriptional regulation. *Nature biotechnology* **33**, 722-729 (2015).
22. N. Koike, S. H. Yoo, H. C. Huang, V. Kumar, C. Lee, T. K. Kim, J. S. Takahashi, Transcriptional architecture and chromatin landscape of the core circadian clock in mammals. *Science* **338**, 349-354 (2012).
23. P. Janich, A. B. Arpat, V. Castelo-Szekely, M. Lopes, D. Gatfield, Ribosome profiling reveals the rhythmic liver translatome and circadian clock regulation by upstream open reading frames. *Genome research* **25**, 1848-1859 (2015).
24. C. E. French, G. Wei, J. P. B. Lloyd, Z. Hu, A. N. Brooks, S. E. Brenner, Transcriptome analysis of alternative splicing-coupled nonsense-mediated mRNA decay in human cells reveals broad regulatory potential. *bioRxiv*, 2020.2007.2001.183327 (2020).
25. M. Stratmann, D. M. Suter, N. Molina, F. Naef, U. Schibler, Circadian Dbp transcription relies on highly dynamic BMAL1-CLOCK interaction with E boxes and requires the proteasome. *Molecular cell* **48**, 277-287 (2012).
26. S. A. Brown, G. Zumbrunn, F. Fleury-Olela, N. Preitner, U. Schibler, Rhythms of mammalian body temperature can sustain peripheral circadian clocks. *Current biology : CB* **12**, 1574-1583 (2002).
27. M. Schuler, A. Dierich, P. Chambon, D. Metzger, Efficient temporally controlled targeted somatic mutagenesis in hepatocytes of the mouse. *Genesis* **39**, 167-172 (2004).
28. S.-H. Yoo, S. Yamazaki, P. L. Lowrey, K. Shimomura, C. H. Ko, E. D. Buhr, S. M. Siepka, H.-K. Hong, W. J. Oh, O. J. Yoo, PERIOD2:: LUCIFERASE real-time reporting of circadian dynamics reveals persistent circadian oscillations in mouse peripheral tissues. *Proceedings of the National Academy of Sciences* **101**, 5339-5346 (2004).
29. J. Aschoff, H. Pohl, Phase relations between a circadian rhythm and its zeitgeber within the range of entrainment. *Naturwissenschaften* **65**, 80-84 (1978).
30. A. E. Granada, G. Bordyugov, A. Kramer, H. Herzel, Human chronotypes from a theoretical perspective. *PloS one* **8**, e59464 (2013).

31. G. Katsioudi, A. Osorio-Forero, F. Sinturel, C. Hagedorn, F. Kreppel, U. Schibler, D. Gatfield, Recording of Diurnal Gene Expression in Peripheral Organs of Mice Using the RT-Biolumicorder. *Methods Mol Biol* **2482**, 217-242 (2022).
32. C. Saini, A. Liani, T. Curie, P. Gos, F. Kreppel, Y. Emmenegger, L. Bonacina, J.-P. Wolf, Y.-A. Poget, P. Franken, Real-time recording of circadian liver gene expression in freely moving mice reveals the phase-setting behavior of hepatocyte clocks. *Genes & development* **27**, 1526-1536 (2013).
33. M. M. Hoekstra, M. Jan, G. Katsioudi, Y. Emmenegger, P. Franken, The sleep-wake distribution contributes to the peripheral rhythms in PERIOD-2. *eLife* **10**, (2021).
34. J. P. Debruyne, E. Noton, C. M. Lambert, E. S. Maywood, D. R. Weaver, S. M. Reppert, A clock shock: mouse CLOCK is not required for circadian oscillator function. *Neuron* **50**, 465-477 (2006).
35. B. Kornmann, O. Schaad, H. Bujard, J. S. Takahashi, U. Schibler, System-driven and oscillator-dependent circadian transcription in mice with a conditionally active liver clock. *PLoS biology* **5**, e34 (2007).
36. M. Hatano, M. Umemura, N. Kimura, T. Yamazaki, H. Takeda, H. Nakano, S. Takahashi, Y. Takahashi, The 5'-untranslated region regulates ATF5 mRNA stability via nonsense-mediated mRNA decay in response to environmental stress. *The FEBS journal* **280**, 4693-4707 (2013).
37. K. Pakos-Zebrucka, I. Koryga, K. Mnich, M. Ljujic, A. Samali, A. M. Gorman, The integrated stress response. *EMBO Rep* **17**, 1374-1395 (2016).
38. A. Gopalsamy, E. M. Bennett, M. Shi, W. G. Zhang, J. Bard, K. Yu, Identification of pyrimidine derivatives as hSMG-1 inhibitors. *Bioorg Med Chem Lett* **22**, 6636-6641 (2012).
39. L. M. Langer, F. Bonneau, Y. Gat, E. Conti, Cryo-EM reconstructions of inhibitor-bound SMG1 kinase reveal an autoinhibitory state dependent on SMG8. *eLife* **10**, (2021).
40. B. Zinshteyn, N. K. Sinha, S. U. Enam, B. Koleske, R. Green, Translational repression of NMD targets by GIGYF2 and EIF4E2. *PLoS genetics* **17**, e1009813 (2021).
41. G. Wu, R. C. Anafi, M. E. Hughes, K. Kornacker, J. B. Hogenesch, MetaCycle: an integrated R package to evaluate periodicity in large scale data. *Bioinformatics* **32**, 3351-3353 (2016).
42. S. Luck, P. O. Westermark, Circadian mRNA expression: insights from modeling and transcriptomics. *Cellular and molecular life sciences : CMLS* **73**, 497-521 (2016).
43. G. Rey, F. Cesbron, J. Rougemont, H. Reinke, M. Brunner, F. Naef, Genome-wide and phase-specific DNA-binding rhythms of BMAL1 control circadian output functions in mouse liver. *PLoS biology* **9**, e1000595 (2011).
44. A. B. Arpat, A. Liechti, M. De Matos, R. Dreos, P. Janich, D. Gatfield, Transcriptome-wide sites of collided ribosomes reveal principles of translational pausing. *Genome research* **30**, 985-999 (2020).
45. F. Schueren, T. Lingner, R. George, J. Hofhuis, C. Dickel, J. Gartner, S. Thoms, Peroxisomal lactate dehydrogenase is generated by translational readthrough in mammals. *eLife* **3**, e03640 (2014).
46. F. Damiola, N. Le Minh, N. Preitner, B. Kornmann, F. Fleury-Olela, U. Schibler, Restricted feeding uncouples circadian oscillators in peripheral tissues from the central pacemaker in the suprachiasmatic nucleus. *Genes & development* **14**, 2950-2961 (2000).
47. R. Chavan, C. Feillet, S. S. Costa, J. E. Delorme, T. Okabe, J. A. Ripperger, U. Albrecht, Liver-derived ketone bodies are necessary for food anticipation. *Nature communications* **7**, 10580 (2016).
48. S. Miller, Y. L. Son, Y. Aikawa, E. Makino, Y. Nagai, A. Srivastava, T. Oshima, A. Sugiyama, A. Hara, K. Abe, Isoform-selective regulation of mammalian cryptochromes. *Nature chemical biology* **16**, 676-685 (2020).
49. S. N. Anand, E. S. Maywood, J. E. Chesham, G. Joynson, G. T. Banks, M. H. Hastings, P. M. Nolan, Distinct and separable roles for endogenous CRY1 and CRY2 within the circadian

molecular clockwork of the suprachiasmatic nucleus, as revealed by the Fbxl3Afh mutation. *Journal of Neuroscience* **33**, 7145-7153 (2013).
50. M. Ukai-Tadenuma, R. G. Yamada, H. Xu, J. A. Ripperger, A. C. Liu, H. R. Ueda, Delay in feedback repression by cryptochrome 1 is required for circadian clock function. *Cell* **144**, 268-281 (2011).
51. A. C. Liu, D. K. Welsh, C. H. Ko, H. G. Tran, E. E. Zhang, A. A. Priest, E. D. Buhr, O. Singer, K. Meeker, I. M. Verma, Intercellular coupling confers robustness against mutations in the SCN circadian clock network. *Cell* **129**, 605-616 (2007).
52. K. A. Stokkan, S. Yamazaki, H. Tei, Y. Sakaki, M. Menaker, Entrainment of the circadian clock in the liver by feeding. *Science* **291**, 490-493 (2001).
53. P. Crosby, R. Hamnett, M. Putker, N. P. Hoyle, M. Reed, C. J. Karam, E. S. Maywood, A. Stangherlin, J. E. Chesham, E. A. Hayter, L. Rosenbrier-Ribeiro, P. Newham, H. Clevers, D. A. Bechtold, J. S. O'Neill, Insulin/IGF-1 Drives PERIOD Synthesis to Entrain Circadian Rhythms with Feeding Time. *Cell* **177**, 896-909 e820 (2019).
54. J. O. Lipton, E. D. Yuan, L. M. Boyle, D. Ebrahimi-Fakhari, E. Kwiatkowski, A. Nathan, T. Guttler, F. Davis, J. M. Asara, M. Sahin, The Circadian Protein BMAL1 Regulates Translation in Response to S6K1-Mediated Phosphorylation. *Cell* **161**, 1138-1151 (2015).
55. N. Velingkaar, V. Mezhnina, A. Poe, R. V. Kondratov, Two-meal caloric restriction induces 12-hour rhythms and improves glucose homeostasis. *FASEB journal : official publication of the Federation of American Societies for Experimental Biology* **35**, e21342 (2021).
56. R. V. Khapre, A. A. Kondratova, S. Patel, Y. Dubrovsky, M. Wrobel, M. P. Antoch, R. V. Kondratov, BMAL1-dependent regulation of the mTOR signaling pathway delays aging. *Aging (Albany NY)* **6**, 48-57 (2014).
57. R. Wu, F. Dang, P. Li, P. Wang, Q. Xu, Z. Liu, Y. Li, Y. Wu, Y. Chen, Y. Liu, The Circadian Protein Period2 Suppresses mTORC1 Activity via Recruiting Tsc1 to mTORC1 Complex. *Cell metabolism* **29**, 653-667 e656 (2019).
58. A. Gonzalez, M. N. Hall, Nutrient sensing and TOR signaling in yeast and mammals. *The EMBO journal* **36**, 397-408 (2017).
59. S. R. Jaffrey, M. F. Wilkinson, Nonsense-mediated RNA decay in the brain: emerging modulator of neural development and disease. *Nature Reviews Neuroscience* **19**, 715-728 (2018).
60. M. W. Popp, L. E. Maquat, Nonsense-mediated mRNA decay and cancer. *Current opinion in genetics & development* **48**, 44-50 (2018).
61. B. Maier, S. Wendt, J. T. Vanselow, T. Wallach, S. Reischl, S. Oehmke, A. Schlosser, A. Kramer, A large-scale functional RNAi screen reveals a role for CK2 in the mammalian circadian clock. *Genes & development* **23**, 708-718 (2009).
62. T. Bording, A. N. Abdo, B. Maier, C. Gabriel, A. Kramer, Generation of Human CRY1 and CRY2 Knockout Cells Using Duplex CRISPR/Cas9 Technology. *Front Physiol* **10**, 577 (2019).
63. C. H. Gabriel, M. Del Olmo, A. Zehtabian, M. Jager, S. Reischl, H. van Dijk, C. Ulbricht, A. Rakhymzhan, T. Korte, B. Koller, A. Grudziecki, B. Maier, A. Herrmann, R. Niesner, T. Zemojtel, H. Ewers, A. E. Granada, H. Herzel, A. Kramer, Live-cell imaging of circadian clock protein dynamics in CRISPR-generated knock-in cells. *Nature communications* **12**, 3796 (2021).
64. A. Dobin, C. A. Davis, F. Schlesinger, J. Drenkow, C. Zaleski, S. Jha, P. Batut, M. Chaisson, T. R. Gingeras, STAR: ultrafast universal RNA-seq aligner. *Bioinformatics* **29**, 15-21 (2013).
65. S. Anders, P. T. Pyl, W. Huber, HTSeq—a Python framework to work with high-throughput sequencing data. *bioinformatics* **31**, 166-169 (2015).
66. P. Danecek, J. K. Bonfield, J. Liddle, J. Marshall, V. Ohan, M. O. Pollard, A. Whitwham, T. Keane, S. A. McCarthy, R. M. Davies, Twelve years of SAMtools and BCFtools. *Gigascience* **10**, giab008 (2021).

67. M. I. Love, W. Huber, S. Anders, Moderated estimation of fold change and dispersion for RNA-seq data with DESeq2. *Genome biology* **15**, 1-21 (2014).
68. M. Brancaccio, M. D. Edwards, A. P. Patton, N. J. Smyllie, J. E. Chesham, E. S. Maywood, M. H. Hastings, Cell-autonomous clock of astrocytes drives circadian behavior in mammals. *Science* **363**, 187-192 (2019).
69. J. T. Ting, B. R. Lee, P. Chong, G. Soler-Llavina, C. Cobbs, C. Koch, H. Zeng, E. Lein, Preparation of acute brain slices using an optimized N-methyl-D-glucamine protective recovery method. *JoVE (Journal of Visualized Experiments)*, e53825 (2018).
70. D. J. Lavery, U. Schibler, Circadian transcription of the cholesterol 7 alpha hydroxylase gene may involve the liver-enriched bZIP protein DBP. *Genes & development* **7**, 1871-1884 (1993).

Acknowledgements

We thank the Lausanne Genomic Technologies Facility for library preparation and sequencing, Paul Franken and Yann Emmenegger for equipment and help with *in vivo* experiments, Oliver Mühlemann for SMG1i compound, and Aleksandar Vjestica and Niels Gehring for valuable comments on the manuscript.

Funding:

Swiss National Science Foundation (SNSF), NCCR RNA & Disease grant 141735 (DG)

Swiss National Science Foundation (SNSF) individual grant 179190 (DG)

Swiss National Science Foundation (SNSF) individual grant 179313 (SAB)

German Research Foundation (DFG) grant 278001972 - TRR 186 (AK)

Velux Foundation grant 985 (SAB)

Canon Research Fellowship (MS)

Author contributions:

Conceptualisation: DG, GK, RD

Methodology: GK, RD, SG, MS, CHG

Investigation: GK, RD, ESA, SG, AL, MS, CHG

Visualisation: GK, RD, ESA, SG, MS, CHG, DG

Supervision: DG, AK, SAB

Writing—original draft: DG, GK, RD

Writing—review & editing: SG, CHG, MS, ESA

Competing interests: Authors declare that they have no competing interests.

Data and Materials Availability: All data needed to evaluate the conclusions in the paper are present in the paper and/or the Supplementary Materials. Sequencing data have been deposited at GEO (GSE208769). Computational code is accessible at Zenodo under 10.5281/zenodo.7347614 (link: https://doi.org/10.5281/zenodo.7347614) and at https://github.com/talponer/smg6ExpressionData.

Supplementary Materials

The pdf file contains: Figs. S1 to S3.

Figure Legends

Figure 1. A novel conditional NMD loss-of-function allele based on *Smg6* PIN nuclease domain mutation.

(**A**) Schematic of the genetic model. *Smg6*^{flox} expresses wild-type SMG6 protein encoded by the blue exons; after Cre-mediated recombination to *Smg6*^{mut}, point-mutated exons 18 and 19 (yellow) lead to expression of mutant SMG6 (D1352A, D1391A).

(**B**) The mutated aspartic acid residues (marked red) are within the catalytic triade of the PIN nuclease domain, shown here in the structure of the human protein (PDB accession 2HWW; (18)). In the mouse protein, human Asp1392 is at position 1391, and human Asp1353 at 1352.

(**C**) For cellular studies, tail fibroblasts from adult male mice (*Smg6*^{flox} and wild-type littermates) were cultured until spontaneous immortalisation, and tamoxifen-activatable CreERT2 expression was achieved by a retrovirus. Upon 4-hydroxytamoxifen (4-OHT) treatment, NMD mutants (yellow) were compared to different control cells (shades of blue).

(**D**) PCR-based genotyping of genomic DNA extracted from cells depicted in panel (C) indicates efficient recombination upon 4-OHT treatment.

(**E**) A luciferase reporter containing an intron in the 3' UTR is upregulated in 4-OHT-treated *Smg6*$^{flox/flox}$ cells, as expected under NMD-inactive conditions. N=2-6 plates/group, adjusted p=0.038; multiple Student's t-test.

Figure 2. *Smg6* mutation stabilises endogenous NMD targets.

(**A**) Density plot showing transcriptome-wide mRNA/pre-mRNA ratio distributions calculated from RNA-seq, in NMD-inactive (yellow) vs. control cells (shades of blue).

(**B**) The difference in mRNA/pre-mRNA ratios between NMD-inactivated (*Smg6*$^{flox/flox}$ + 4-OHT) and control cells (*Smg6*$^{flox/flox}$ + vehicle) is consistent with higher stability of annotated NMD substrates (purple, N=2681) and transcripts with retained introns (green, N=3369). Moreover, the broad distribution and shift to positive values for not previously NMD-annotated protein coding transcripts (beige, N=3232) is indicative of transcriptome-wide mRNA stability increase and NMD regulation.

(**C**) Read coverage on the *Hnrnpl* and (**D**) *Srsf11* loci indicates the specific upregulation of transcript isoforms that are NMD-annotated (purple) and that can be identified via specific exons (marked by arrows in insets).

(**E**) Differential expression analysis at the exon level, comparing *Smg6*$^{flox/flox}$ + 4-OHT vs. *Smg6*$^{flox/flox}$ + vehicle conditions, reveals significant upregulation of NMD-annotated exons (purple; N=492; 169 genes), retained introns (green; N=521; 122 genes), and a sizeable

number of constitutive exons (beige; N=1787; 382 genes), suggestive of NMD regulating many protein-coding genes.

(**F**) Correlation analysis between mRNA/pre-mRNA ratio change upon NMD inactivation vs. expression levels in wild-type cells shows significant anticorrelation.

(**G**) The lengths of 5' UTRs, (**H**) CDS and (**I**) 3' UTRs are all positively correlated with mRNA/pre-mRNA ratio change upon NMD inactivation. Pearson correlation coefficient (r), slope and p-values were calculated by a linear model and indicated in the panels.

Figure 3. *Smg6* mutation lengthens free-running circadian periods.

(**A**) Bioluminescence rhythms *(Dbp-Luciferase)* of mutant and control fibroblasts under free-running conditions after temperature-entrainment; representative traces from $Smg6^{mut}$ (yellow; 4-OHT) and $Smg6^{flox/flox}$ (blue, no 4-OHT) cells.

(**B**) Period length quantification of several experiments as in (A) with $Smg6^{mut}$ (yellow; 4-OHT), $Smg6^{flox/flox}$ (blue; no 4-OHT) and $Smg6^{+/+}$ with/without 4-OHT (grey). N=3-5; $Smg6^{mut}$ vs $Smg6^{flox/flox}$ period difference is 1.6h; Bonferroni's multiple comparisons test adjusted p=0.0228.

(**C**) Liver and kidney explants from littermate adult mice were excised for bioluminescence recording. Representative traces from $Smg6^{mut}$ (yellow) and control (blue) livers.

(**D**) Quantification of experiments as in (C). Long periods (values: mean ± SD) were observed in NMD-deficient liver explants (yellow; 25.36 ± 2.23h) compared to control livers (blue; 22.0 ± 0.90h). Kidney explants from same animals in grey ($Smg6^{flox/flox}$: 25.2 ± 1.19h; $Smg6^{+/+}$: 24.4 ± 1.83h). Livers: N=16-17; Mann-Whitney test p<0.0001. Kidney: N=16-20; p=0.0771. 1-4 tissue slices/mouse; blind analyses.

(**E**) Cartoon depicting the *in vivo* recording setup (RT-Biolumicorder).

(**F**) Left: Bioluminescence rhythms and activity were recorded under skeleton photoperiod (yellow vertical lines at ZT0 and before ZT12). Mean signal (solid trace) and SEM (shaded) over the whole course of the experiment. Right: Compiled data of all mice, averaged from day 3, for tamoxifen-injected $Smg6^{flox/flox}$ (yellow) and $Smg6^{+/+}$ (blue) animals, all carrying $Alb^{CreERT2}$ and *mPer2::Luc*.

(**G**) Quantification of PER2::LUC bioluminescence peak phase difference between mutants (yellow) and controls (blue). N=6; Mann-Whitney test p=0.7251.

(**H**) Liver genotyping confirms efficient recombination (PCR on genomic DNA).

Figure 4. *Smg6* mutation differentially affects hepatic core clock pre-mRNA and mRNA rhythms.

(**A**) Schematic of the around-the-clock RNA-seq experiment, which was carried out on a time series of liver samples collected from LD12:12-entrained male *Smg6* mutant (*Smg6*$^{flox/flox}$; *Alb*^{CreERT2}; tamoxifen-treated) and control (*Smg6*$^{+/+}$; *Alb*^{CreERT2}; tamoxifen-treated) mice.

(**B**)-(**J**) RNA-seq data is plotted for indicated core clock genes for mRNA (upper panels; exonic reads) and pre-mRNA (lower panels; intronic reads) for *Smg6* mutants (yellow) and controls (blue). RPKM values (Reads Per Kilobase of transcript, per Million mapped reads) of individual mouse livers are shown as dots with solid lines connecting the means for each timepoint. The dashed lines represent the rhythmic data fit using the parameters from MetaCycle (*41*).

(**K**) Circular plot representing the phases of peak mRNA abundances according to the MetaCycle fits for *Smg6* mutants (dashed) and controls (solid) for indicated core clock genes. *Cry2*, *Nr1d2* and *Ror*γ accumulated several hours later in *Smg6* mutants, whereas minor effects were seen for other genes.

(**L**) Same analysis as in (K) for pre-mRNA rhythms. Several core clock pre-mRNAs showed later phases, indicative of transcriptional shifts; notable exceptions being *Per2* (almost invariable), and *Cry2* and *Nr1d2* that both showed a phase advance.

(**M**) Similar to Fig. 2, mRNA/pre-mRNA ratios were calculated for the liver RNA-seq data; briefly, average mRNA counts were first averaged over all samples per genotype, before dividing by average pre-mRNA counts. Three components of the negative limb, *Cry2*, *Cry1* and *Per2*, showed higher mRNA/pre-mRNA ratios in *Smg6* mutants.

Figure 5. Endogenous *Cry2* mRNA and protein are sensitive to NMD activity.

(**A**) mRNA/pre-mRNA ratios across individual liver samples – grouped into light (ZT0, 4, 8) and dark phase (ZT12,16, 20) – indicate increased *Cry2* mRNA stability in *Smg6* mutants in the dark phase; p-value=0.06; ANOVA.

(**B**) Western blot analysis of total liver proteins (pool of 3 mice/sample), for CRY2 and HSP90 (loading control).

(**C**) Quantification of Western blot from (B). CRY2 intensity was normalised to HSP90 (loading control).

(**D**) Western blot as in (B), but from individual animals at ZT8 and ZT20; CRY2 is reproducibly more abundant at ZT20 in *Smg6* mutants.

(**E**) Quantification of Western blot in (D); p=0.1; Mann-Whitney non-parametric test.

(**F**) Western blot analysis of total protein from fibroblasts (cells as in Fig. 1C) reveals CRY2 upregulation specifically in 4-OHT-treated *Smg6*$^{flox/flox}$ cells.

(**G**) Quantification of Western blot shown in (F); p=0.002; Mann-Whitney non-parametric test.

(**H**) RNA-seq coverage on *Cry2* locus (fibroblasts). Only the transcript isoform carrying the 2.2 kb (and not the shorter) 3' UTR is expressed.

(**I**) Schematic of the lentiviral dual luciferase system used to test 3' UTRs of interest.

(**J**) Dual-luciferase assays reveal NMD regulation via the *Cry2* 3' UTR. Vector UTR alone shows ca. 5-fold upregulation under *Smg6*$^{flox/flox}$ (+4-OHT) conditions. Against this background, the *Cry2* UTR confers an additional >5-fold increase. Each genotype/reporter condition without 4-OHT treatment was internally set to 1, and the signal of 4-OHT-treated cells relative to these untreated cells is reported; N=5 from 3 different experiments; p=0.001; Mann-Whitney non-parametric test.

Figure 6. NMD regulation of *Cry2* mRNA via its long 3' UTR.

(**A**) Bioluminescence traces of NIH/3t3 cells carrying the *Dbp-Luciferase* reporter gene, with (orange) or without (grey) 0.6 µM SMG1i treatment. Traces show mean ± SD from 3 independent experiments.

(**B**) Quantification of experiments as in (A), showing reproducible period lengthening by ca. 4 h in the presence of 0.6 µM SMG1i (N=11-12; p<0.001; Mann-Whitney test).

(**C**) Western blot analysis of total protein extract from NIH/3t3 cells treated with vehicle or 0.6 µM SMG1i; quantification of CRY2 abundance normalised to HSP90 below lanes.

(**D**) Primary fibroblasts (genotype *Smg6*$^{+/+}$) were stably transduced with luciferase reporters carrying different 3' UTRs, as in Fig. 5J. When in real-time recording a relatively stable state of Firefly luciferase signal was reached, 1 µM SMG1i (orange) or vehicle (grey) were added to cells. The reporter carrying vector 3' UTR was compared to the *Cry2, Per1,* and *Per2* 3' UTRs. Traces show normalised data with mean ± SD; N=3.

(**E**) In assays as in (D), expression levels of full-length *Cry2* 3' UTR were compared to depicted 3' UTR fragments (N=2).

(**F**) Western blot showing absence of CRY2 in Crispr/Cas9-generated *Cry2* knockout NIH/3t3 cells.

(**G**) Period length of *Dbp-Luciferase* traces in NIH/3t3 cells (controls, grey; *Cry2* knockouts, green), treated with indicated concentrations of SMG1i or with vehicle (DMSO; corresponding to the volume used in highest SMG1i treatment).

Figure 7. Altered transcriptome rhythms in entrained *Smg6* mutant livers.

(**A**) Heatmap of transcripts, mRNA rhythmic in both genotypes. Expression levels are represented as Z-scores that were calculated separately for mRNA and pre-mRNA, but on a common scale for both genotypes. Transcripts are phase-ordered using controls.

(**B**) As in (A), mRNA rhythmic only in controls (N=223).

(**C**) As in (A) mRNA rhythmic only in mutants (N=329).

(**D**) Radial diagrams showing peak phase of rhythmic mRNAs in control (blue) and *Smg6* mutant (yellow) livers for transcripts in (A). Dark/light shaded: high/low amplitude, with high/low cut-off on $\log_2$ peak-trough amplitude of 1.

(**E**) Peak phase of mRNA in *Smg6* mutants (yellow) relative to control (blue), ranked according to phase in controls, using transcripts from (A) (N=1257). Data are double-plotted.
(**F**) Mutant vs control peak phase difference for commonly rhythmic mRNAs (N=1257).
(**G**) Peak phase difference of mRNAs with ChIP-seq binding sites for BMAL1 and CLOCK (N=130), according to (*22*); p=0.0065; permutation test, i.e. 1000x subsampling of N=130 transcripts from the "all rhythmic transcripts" (N=1257) of (F), then comparing means of subsampling groups with observed mean (t-test).
(**H**) As in (G), for mRNAs with ChIP-seq sites for PERs and CRYs from (*22*); p=0.0005; permutation test as in (G).
(**I**) As in (G), for rhythmic mRNAs with no ChIP-seq binding sites for any of the proteins BMAL1, CLOCK, PER1, PER2, CRY1 or CRY2; p=0.18; permutation test as in (G).
(**J**) Z-score amplitudes (difference between maximum and minimum Z-score values, calculated independently for mRNAs and pre-mRNAs of commonly rhythmic transcripts; N=1257) show lower mean mRNA (p=0.236) and higher mean pre-mRNA amplitudes in mutants (p=2e-16); significance calculations from a linear model (equivalent to t-test).
(**K**) Transcript mRNA/pre-mRNA Z-score amplitude ratios (from the N=1257 common rhythmic transcripts), stratified by genotype, show decrease in mutants; p=2e-16; Student's t-test.
(**L**) RNA-seq data of indicated genes for mRNA (upper panels; exonic reads) and pre-mRNA (lower panels; intronic reads) for *Smg6* mutants (yellow) and controls (blue). See Fig. 4B-J for details.

Figure 8. Altered food shifting kinetics and entrainment of liver clocks in *Smg6* mutant animals *in vivo*.
(**A**) Schematic of the food shifting experiments in the RT-Biolumicorder setup. Mice of genotype $Smg6^{flox/flox}$ and $Smg6^{+/+}$ – all carrying hepatocyte-specific $Alb^{CreERT2}$ and *Per2::Luc* reporter, and injected with tamoxifen – were compared. During 2 days of recording, animals had free access to food (*ad libitum*) and feeding is thus expected to take place mainly in the dark phase (brown arrows). Access to food is then restricted to the light phase (ZT4-12) for 4 days. During the whole experiment, animals are light-entrained using skeleton photoperiods to keep the SCN clock entrained to a defined LD schedule.
(**B**) RT-Biolumicorder traces of individual mice in the food shifting experiment, showing smoothened bioluminescence rhythms (photons) with each line representing the signal from a control (blue) or a liver-specific *Smg6* mutant (yellow) animal.
(**C**) Compiled data averaged over the last two days of the experiment from the N=3-4 animals shown in panel (B). Mean signal (solid trace) and SEM (shaded). The indicated phase differences are calculated from rhythmic fits to the data.
(**D**) Activity traces (infrared signal) for the mice shown in panel (B).

(**E**) Compiled activity data, averaged over the last two days of the experiment, analogous to panel (C).

Figure 9. Model of the regulation of daily dynamics of CRY2 accumulation through NMD. In the entrained liver clock, *Cry2* mRNA is translated and the protein accumulates with a peak in the dark phase (ZT16 in wild-type). In the absence of a functional NMD pathway, *Cry2* mRNA is stabilised, reaches higher levels, and its translation leads to increased CRY2 at later times (ZT20). The specific phases and states noted at the periphery of the circle (e.g. poised, derepression) refer to the findings and terminology from Koike *et al.* (*22*) on E-box binding of core clock proteins.

Figure 1

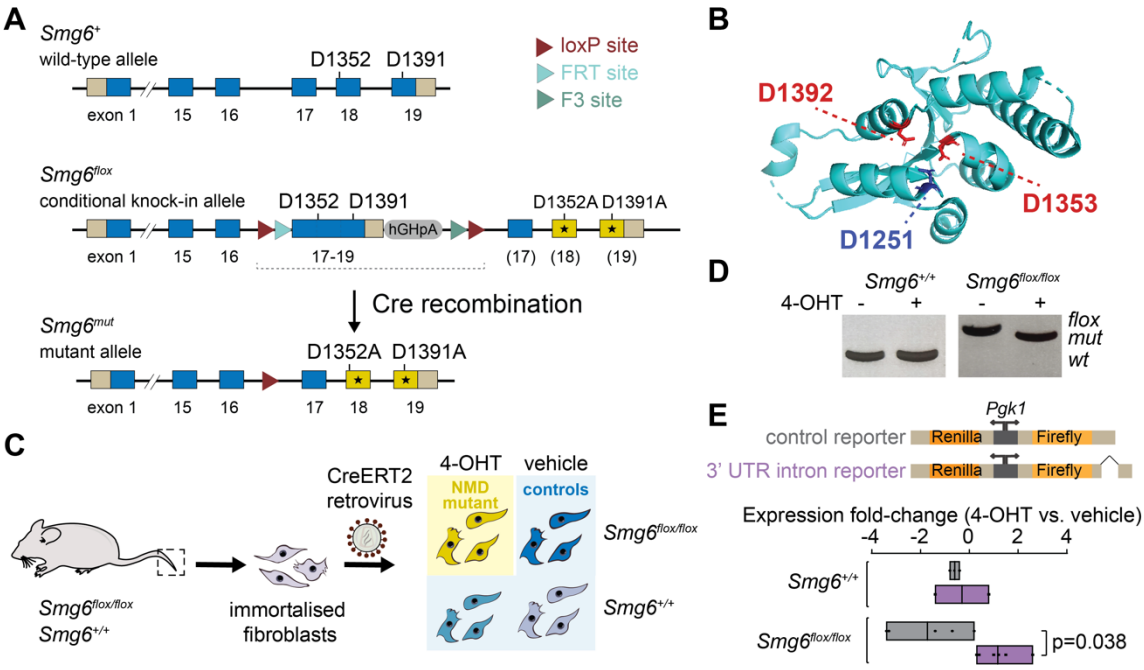
A
Smg6+
wild-type allele
D1352 D1391
exon 1 15 16 17 18 19
loxP site
FRT site
F3 site
Smg6flox
conditional knock-in allele
D1352 D1391
hGHpA
D1352A D1391A
exon 1 15 16 17-19 (17) (18) (19)
Cre recombination
Smg6mut
mutant allele
D1352A D1391A
exon 1 15 16 17 18 19
B
D1392
D1353
D1251
D
Smg6+/+
Smg6flox/flox
4-OHT - + - +
flox
mut
wt
E
Pgk1
control reporter
Renilla
Firefly
3' UTR intron reporter
Renilla
Firefly
Expression fold-change (4-OHT vs. vehicle)
-4 -2 0 2 4
Smg6+/+
Smg6flox/flox
p=0.038
C
4-OHT
vehicle
CreERT2
retrovirus
NMD
mutant
controls
Smg6flox/flox
Smg6+/+
immortalised
fibroblasts
Smg6flox/flox
Smg6+/+

Figure 2

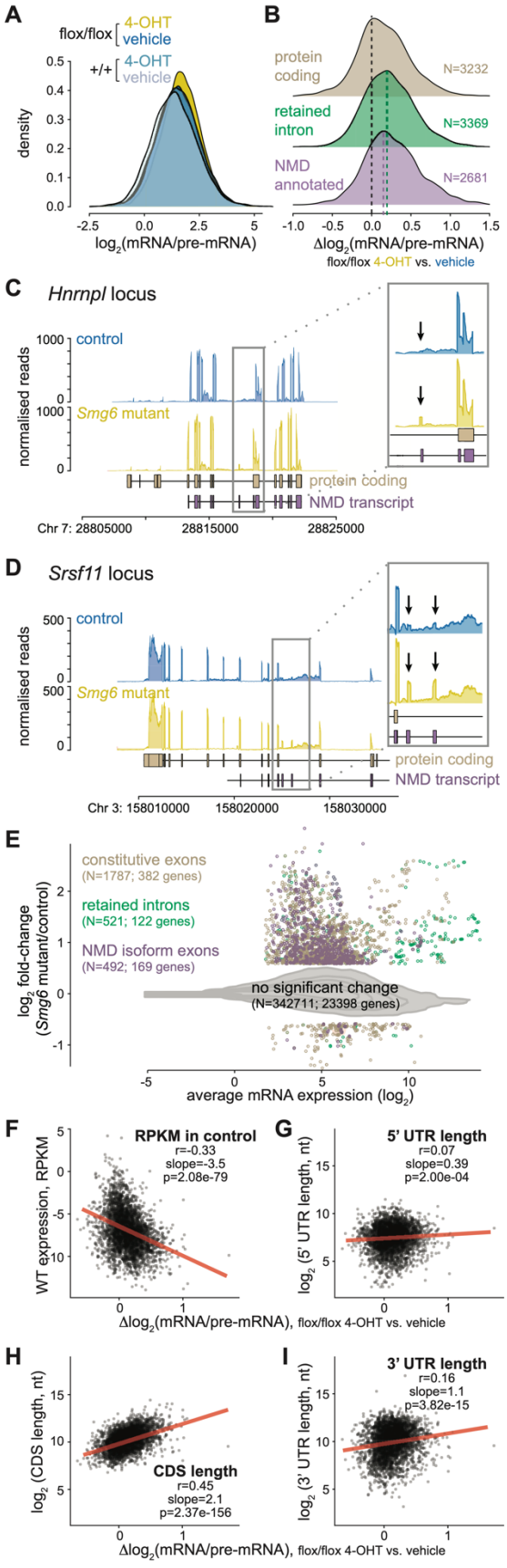
A
flox/flox
4-OHT
vehicle
+/+
4-OHT
vehicle
density
log2(mRNA/pre-mRNA)
B
protein coding
N=3232
retained intron
N=3369
NMD annotated
N=2681
Δlog2(mRNA/pre-mRNA)
flox/flox 4-OHT vs. vehicle
C
Hnrnpl locus
control
Smg6 mutant
normalised reads
protein coding
NMD transcript
Chr 7: 28805000
28815000
28825000
D
Srsf11 locus
control
Smg6 mutant
normalised reads
protein coding
NMD transcript
Chr 3: 158010000
158020000
158030000
E
constitutive exons
(N=1787; 382 genes)
retained introns
(N=521; 122 genes)
NMD isoform exons
(N=492; 169 genes)
no significant change
(N=342711; 23398 genes)
log2 fold-change
(Smg6 mutant/control)
average mRNA expression (log2)
F
RPKM in control
r=-0.33
slope=-3.5
p=2.08e-79
WT expression, RPKM
G
5' UTR length
r=0.07
slope=0.39
p=2.00e-04
log2 (5' UTR length, nt)
Δlog2(mRNA/pre-mRNA), flox/flox 4-OHT vs. vehicle
H
CDS length
r=0.45
slope=2.1
p=2.37e-156
log2 (CDS length, nt)
I
3' UTR length
r=0.16
slope=1.1
p=3.82e-15
log2 (3' UTR length, nt)
Δlog2(mRNA/pre-mRNA), flox/flox 4-OHT vs. vehicle

Figure 3

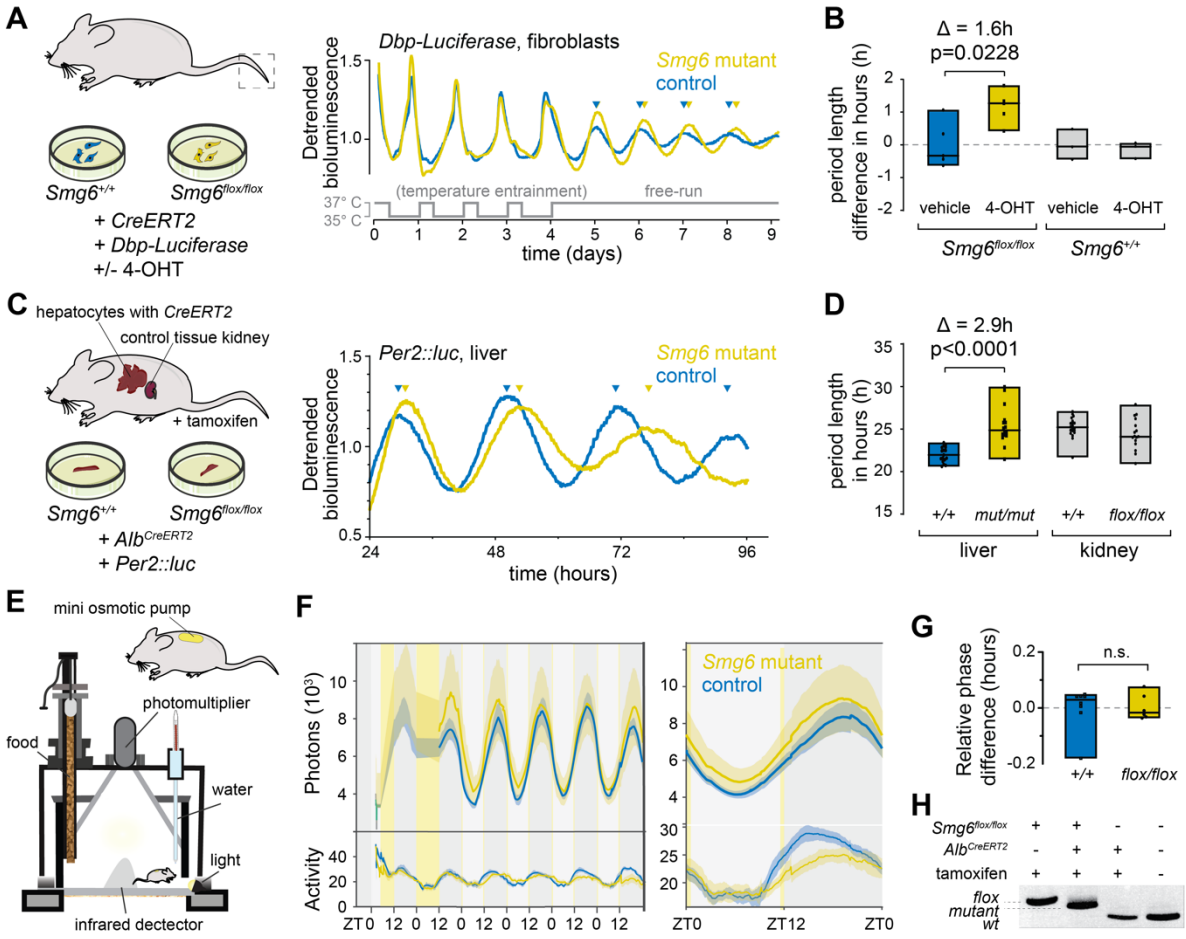
A
Smg6+/+
Smg6flox/flox
+ CreERT2
+ Dbp-Luciferase
+/- 4-OHT
Dbp-Luciferase, fibroblasts
Smg6 mutant
control
Detrended bioluminescence
(temperature entrainment)
free-run
37° C
35° C
time (days)
B
Δ = 1.6h
p=0.0228
period length difference in hours (h)
vehicle
4-OHT
vehicle
4-OHT
Smg6flox/flox
Smg6+/+
C
hepatocytes with CreERT2
control tissue kidney
+ tamoxifen
Smg6+/+
Smg6flox/flox
+ AlbCreERT2
+ Per2::luc
Per2::luc, liver
Smg6 mutant
control
Detrended bioluminescence
time (hours)
D
Δ = 2.9h
p<0.0001
period length in hours (h)
+/+
mut/mut
+/+
flox/flox
liver
kidney
E
mini osmotic pump
photomultiplier
food
water
light
infrared dectector
F
Photons (10³)
Activity
ZT0 12 0 12 0 12 0 12 0 12 0 12
Smg6 mutant
control
ZT0
ZT12
ZT0
G
Relative phase difference (hours)
n.s.
+/+
flox/flox
H
Smg6flox/flox
AlbCreERT2
tamoxifen
flox
mutant
wt

Figure 4

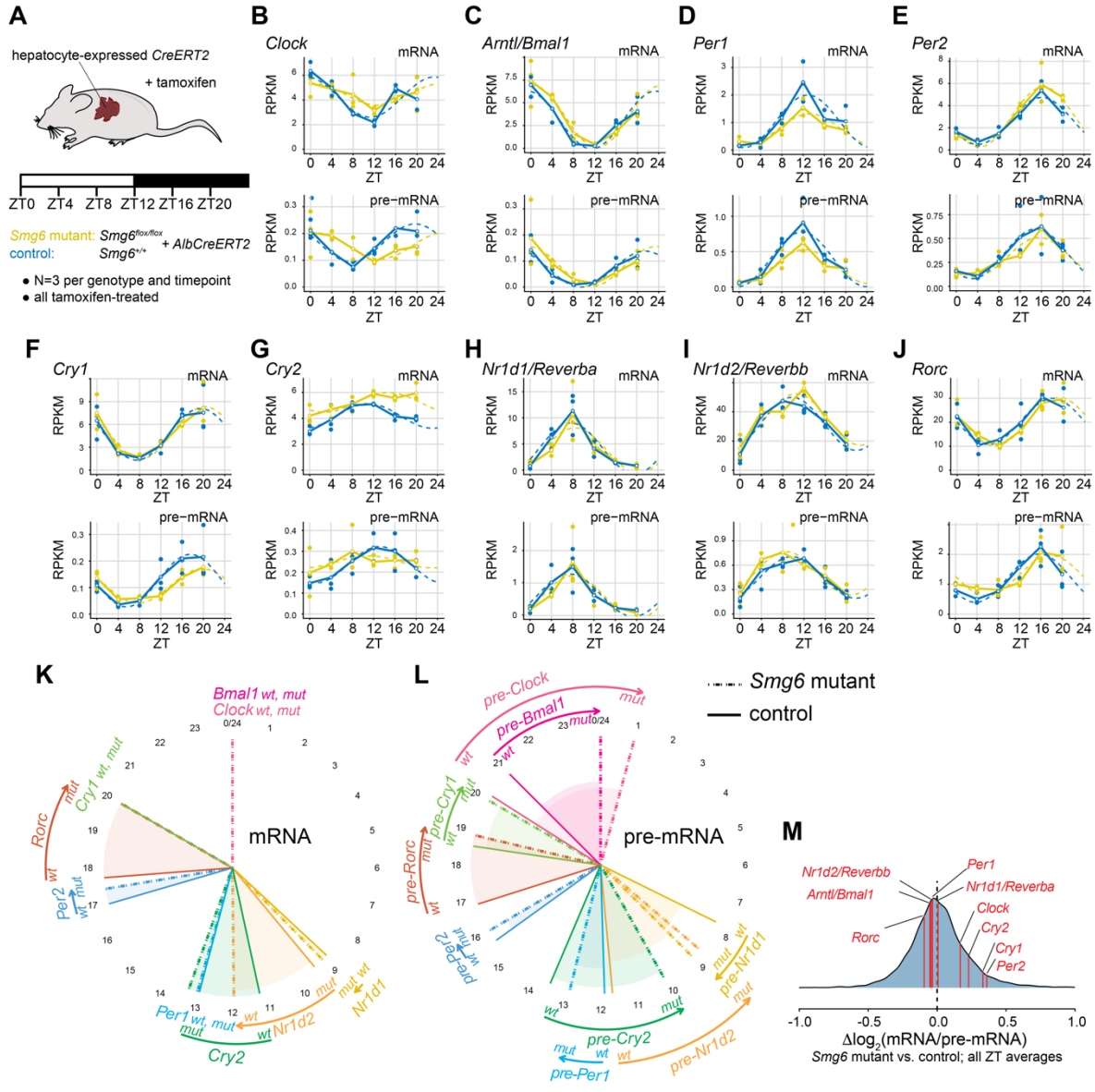
A
hepatocyte-expressed CreERT2
+ tamoxifen
ZT0 ZT4 ZT8 ZT12 ZT16 ZT20
Smg6 mutant: Smg6flox/flox + AlbCreERT2
control: Smg6+/+
• N=3 per genotype and timepoint
• all tamoxifen-treated
B Clock
C Arntl/Bmal1
D Per1
E Per2
F Cry1
G Cry2
H Nr1d1/Reverba
I Nr1d2/Reverbb
J Rorc
mRNA
pre-mRNA
RPKM
ZT
K
L
Smg6 mutant
control
mRNA
pre-mRNA
M
Nr1d2/Reverbb
Arntl/Bmal1
Rorc
Per1
Nr1d1/Reverba
Clock
Cry2
Cry1
Per2
Δlog2(mRNA/pre-mRNA)
Smg6 mutant vs. control; all ZT averages

Figure 5

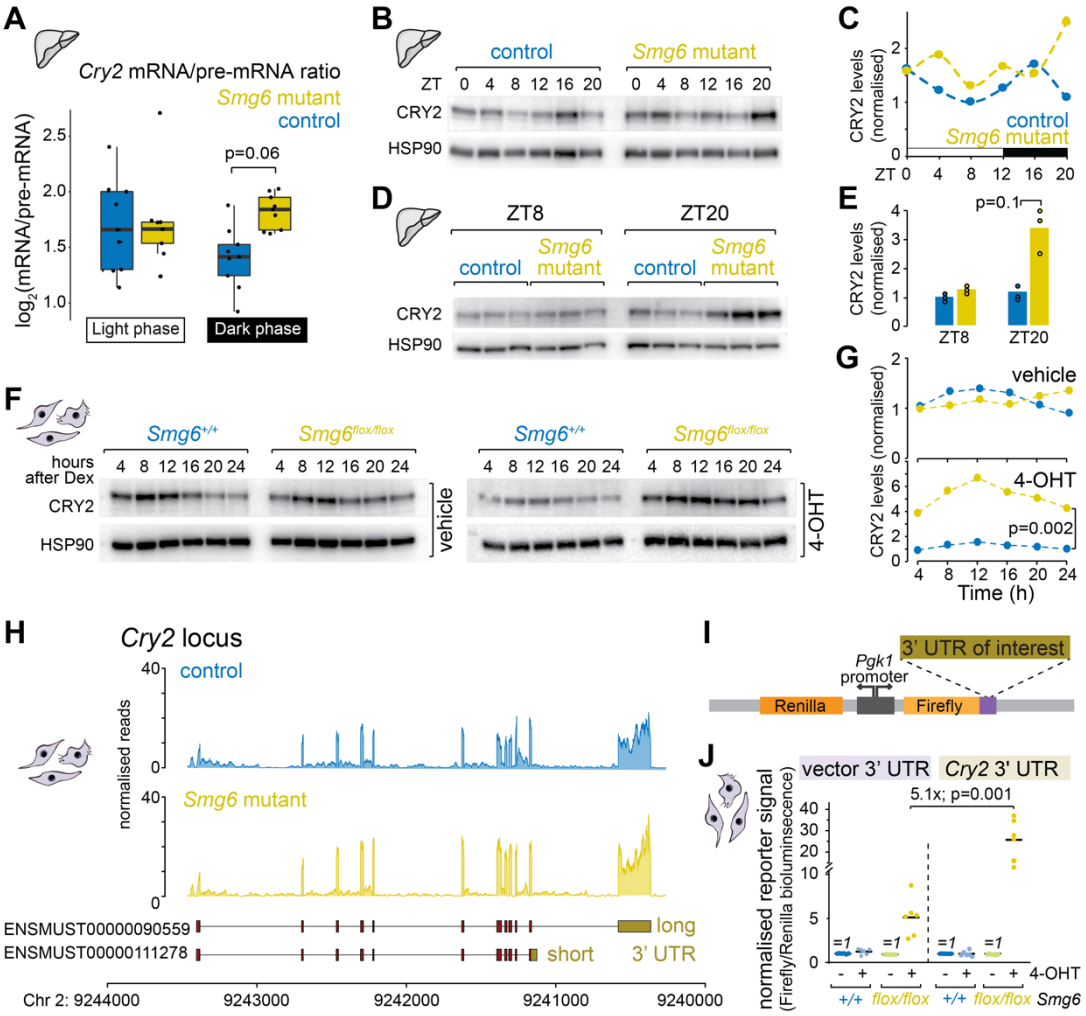
A
Cry2 mRNA/pre-mRNA ratio
Smg6 mutant
control
log2(mRNA/pre-mRNA)
p=0.06
Light phase
Dark phase
B
control
Smg6 mutant
ZT 0 4 8 12 16 20 0 4 8 12 16 20
CRY2
HSP90
C
CRY2 levels (normalised)
control
Smg6 mutant
ZT 0 4 8 12 16 20
D
ZT8
ZT20
control
Smg6 mutant
CRY2
HSP90
E
p=0.1
CRY2 levels (normalised)
ZT8
ZT20
F
Smg6+/+
Smg6flox/flox
hours after Dex
4 8 12 16 20 24
CRY2
HSP90
vehicle
4-OHT
G
vehicle
4-OHT
p=0.002
CRY2 levels (normalised)
Time (h)
H
Cry2 locus
control
Smg6 mutant
normalised reads
ENSMUST00000090559
ENSMUST00000111278
long
short
3' UTR
Chr 2: 9244000
9243000
9242000
9241000
9240000
I
3' UTR of interest
Pgk1 promoter
Renilla
Firefly
J
vector 3' UTR
Cry2 3' UTR
5.1x; p=0.001
normalised reporter signal (Firefly/Renilla bioluminescence)
=1
4-OHT
+/+ flox/flox +/+ flox/flox Smg6

Figure 6

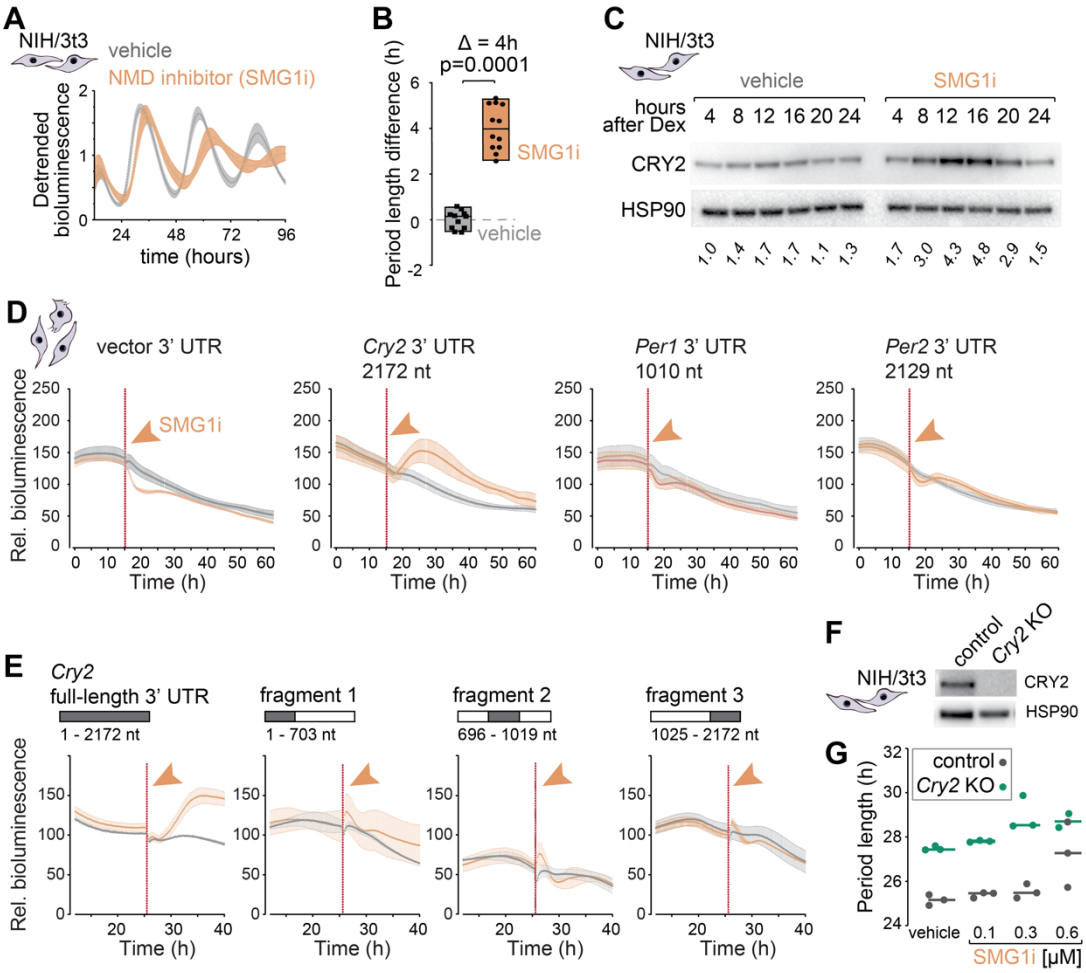
A
NIH/3t3
vehicle
NMD inhibitor (SMG1i)
Detrended bioluminescence
time (hours)
B
Δ = 4h
p=0.0001
SMG1i
vehicle
Period length difference (h)
C
NIH/3t3
vehicle
SMG1i
hours after Dex
4 8 12 16 20 24
4 8 12 16 20 24
CRY2
HSP90
1.0 1.4 1.7 1.7 1.1 1.3
1.7 3.0 4.3 4.8 2.9 1.5
D
vector 3' UTR
Cry2 3' UTR 2172 nt
Per1 3' UTR 1010 nt
Per2 3' UTR 2129 nt
SMG1i
Rel. bioluminescence
Time (h)
E
Cry2
full-length 3' UTR
1 - 2172 nt
fragment 1
1 - 703 nt
fragment 2
696 - 1019 nt
fragment 3
1025 - 2172 nt
Rel. bioluminescence
Time (h)
F
control
Cry2 KO
NIH/3t3
CRY2
HSP90
G
control
Cry2 KO
Period length (h)
vehicle 0.1 0.3 0.6
SMG1i [μM]

Figure 7

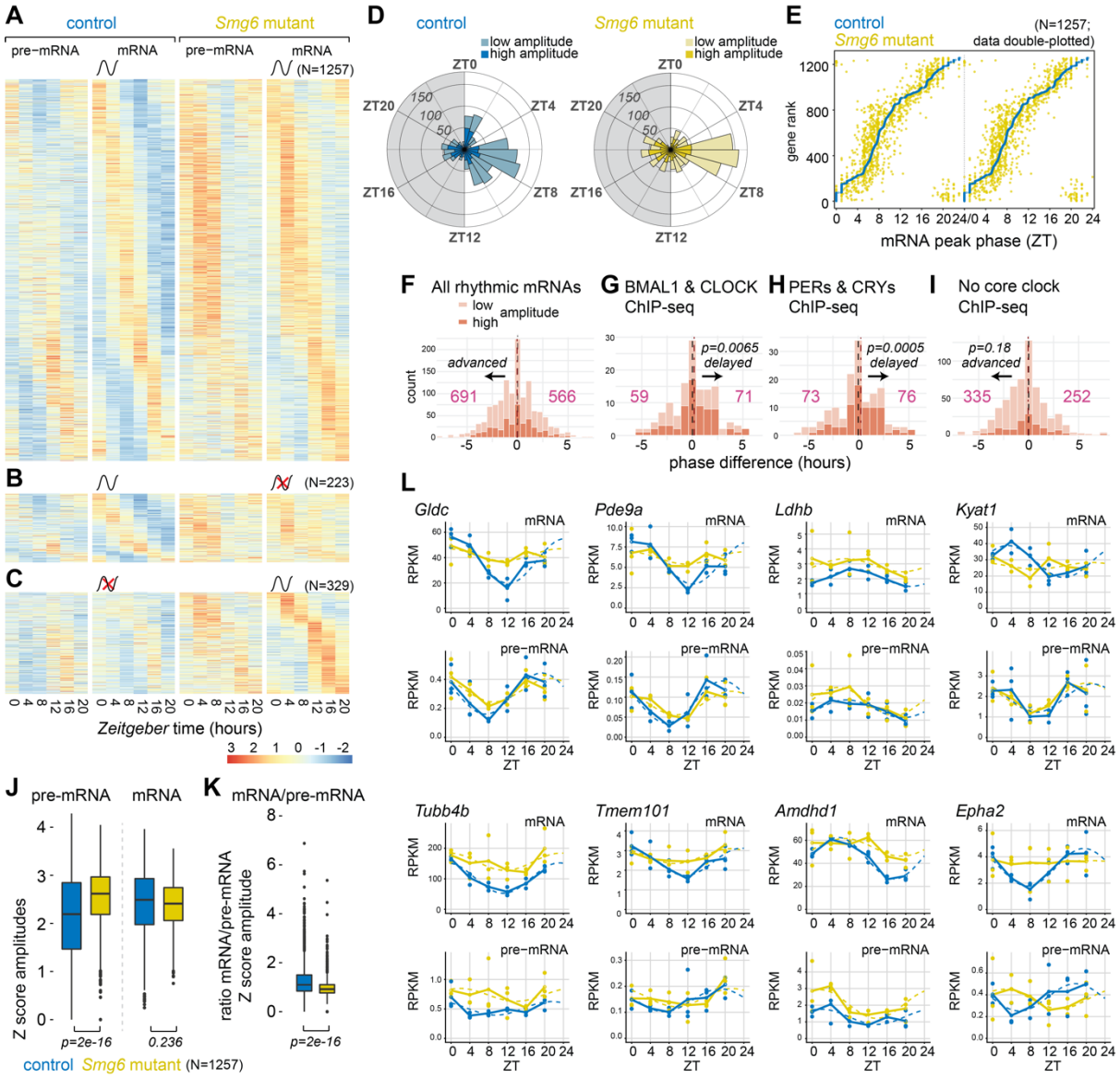
A
control
Smg6 mutant
pre−mRNA
mRNA
(N=1257)
B
(N=223)
C
(N=329)
Zeitgeber time (hours)
D
low amplitude
high amplitude
ZT0
ZT4
ZT8
ZT12
ZT16
ZT20
E
(N=1257;
data double-plotted)
gene rank
mRNA peak phase (ZT)
F
All rhythmic mRNAs
low amplitude
high
count
advanced
691
566
G
BMAL1 & CLOCK
ChIP-seq
p=0.0065
delayed
59
71
H
PERs & CRYs
ChIP-seq
p=0.0005
delayed
73
76
I
No core clock
ChIP-seq
p=0.18
advanced
335
252
phase difference (hours)
J
Z score amplitudes
p=2e-16
0.236
K
mRNA/pre-mRNA
ratio mRNA/pre-mRNA
Z score amplitude
p=2e-16
control Smg6 mutant (N=1257)
L
Gldc
Pde9a
Ldhb
Kyat1
Tubb4b
Tmem101
Amdhd1
Epha2
RPKM
ZT

Figure 8

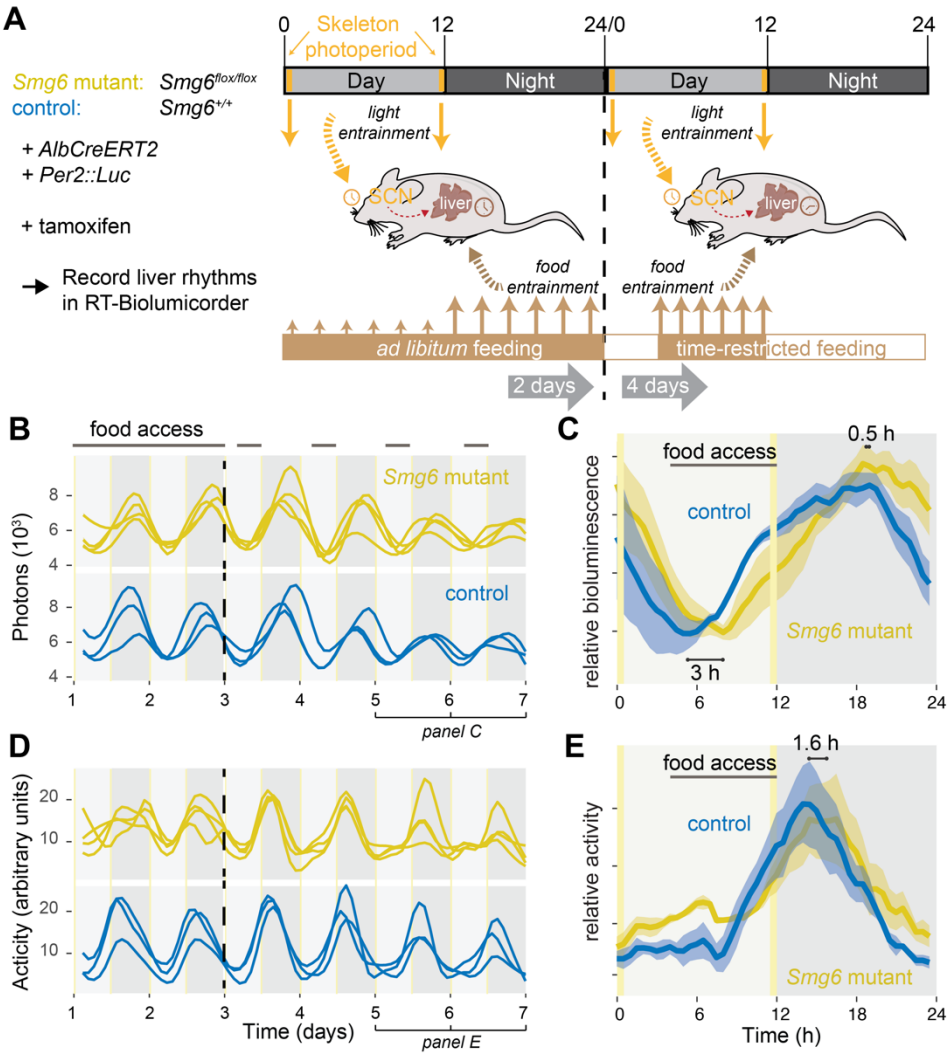
A
0
Skeleton photoperiod
12
24/0
12
24
Day
Night
Day
Night
Smg6 mutant: Smg6flox/flox
control: Smg6+/+
+ AlbCreERT2
+ Per2::Luc
+ tamoxifen
Record liver rhythms in RT-Biolumicorder
light entrainment
light entrainment
SCN
liver
SCN
liver
food entrainment
food entrainment
ad libitum feeding
time-restricted feeding
2 days
4 days
B
food access
Smg6 mutant
control
Photons (10³)
panel C
C
food access
0.5 h
control
Smg6 mutant
3 h
relative bioluminescence
D
Acticity (arbitrary units)
Time (days)
panel E
E
food access
1.6 h
control
Smg6 mutant
relative activity
Time (h)

Figure 9

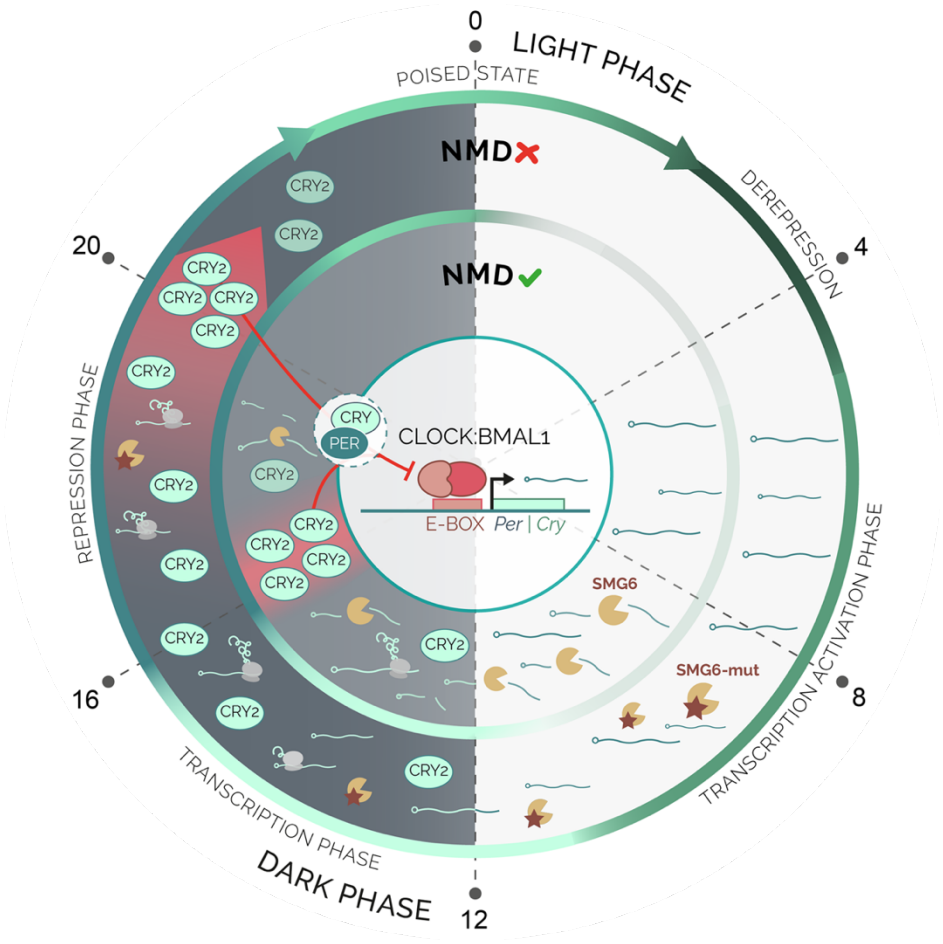
0
LIGHT PHASE
POISED STATE
NMD
NMD
DEREPRESSION
4
20
REPRESSION PHASE
CRY2
CRY
PER
CLOCK:BMAL1
E-BOX Per | Cry
SMG6
SMG6-mut
16
8
TRANSCRIPTION PHASE
TRANSCRIPTION ACTIVATION PHASE
DARK PHASE
12

SUPPLEMENTARY MATERIAL

A novel *Smg6* mouse model reveals circadian clock regulation through the nonsense-mediated mRNA decay pathway

Georgia Katsioudi[1], René Dreos[1], Enes S. Arpa[1], Sevasti Gaspari[1], Angelica Liechti[1], Miho Sato[2], Christian H. Gabriel[3], Achim Kramer[3], Steven A. Brown[2], David Gatfield[1*]

[1] Center for Integrative Genomics, University of Lausanne, Lausanne, Switzerland

[2] Chronobiology and Sleep Research Group, Institute of Pharmacology and Toxicology, University of Zürich, Zürich, Switzerland

[3] Charité Universitätsmedizin Berlin, corporate member of Freie Universität Berlin, Humboldt-Universität zu Berlin, and Berlin Institute of Health, Laboratory of Chronobiology, Berlin, Germany

[*]corresponding author: david.gatfield@unil.ch

Short title: *NMD regulation of the mammalian circadian clock*

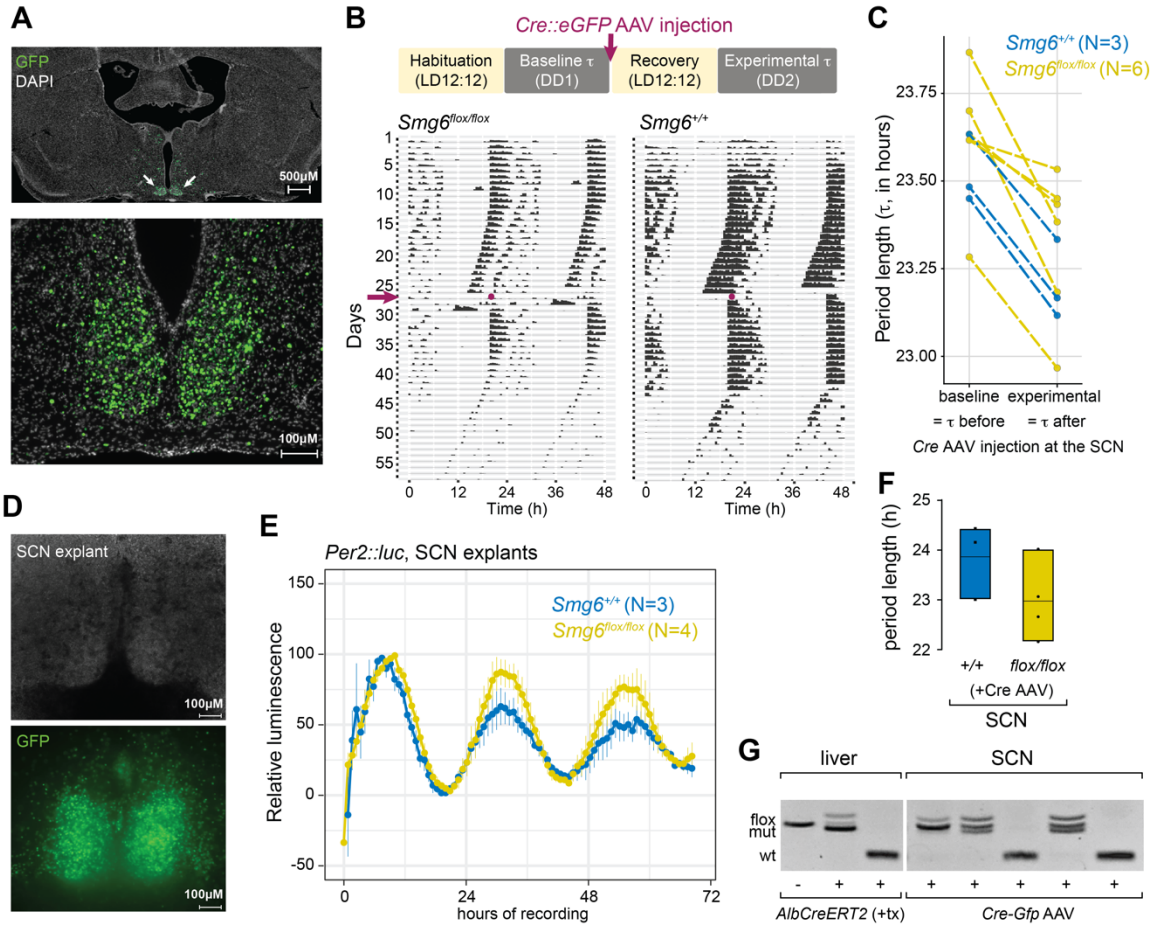

Supplementary Figure S1. (**A**) Representative microphotographs of SCN sections to assess effective targeting of the SCN. Viral expression can be estimated from GFP signal, encoded together with Cre on the same virus. (**B**) Same as (A), but image taken during bioluminescence recording of SCN slices. (**C**) Upper diagram: Rhythms of voluntary locomotor activity were recorded prior to and after the SCN injection of the Cre- and GFP-expressing AAV. Lower: Representative actograms of a *Smg6*$^{flox/flox}$ and *Smg6*$^{+/+}$ mouse. The day of Cre::eGFP AAV injection is marked by an arrow and a dot. (**D**) Period lengths of circadian locomotor activity rhythms of *Smg6*$^{flox/flox}$ (in yellow) and *Smg6*$^{+/+}$ (in blue) mice before (DD1) and after (DD2) stereotaxic surgery. (**E**) Averaged traces of *mPer2::Luc* rhythms of AAV-injected *Smg6*$^{flox/flox}$ (yellow) and *Smg6*$^{+/+}$ (blue) SCN explants. (**F**) Period lengths of *mPer::Luc* expression in AAV-injected *Smg6*$^{flox/flox}$ (yellow) and *Smg6*$^{+/+}$ (blue) SCN explants. (**G**) Recombination efficiency following Cre induction was evaluated by genotyping of genomic DNA extracted from SCN slices (liver-specific mutants served as controls for the genotyping).

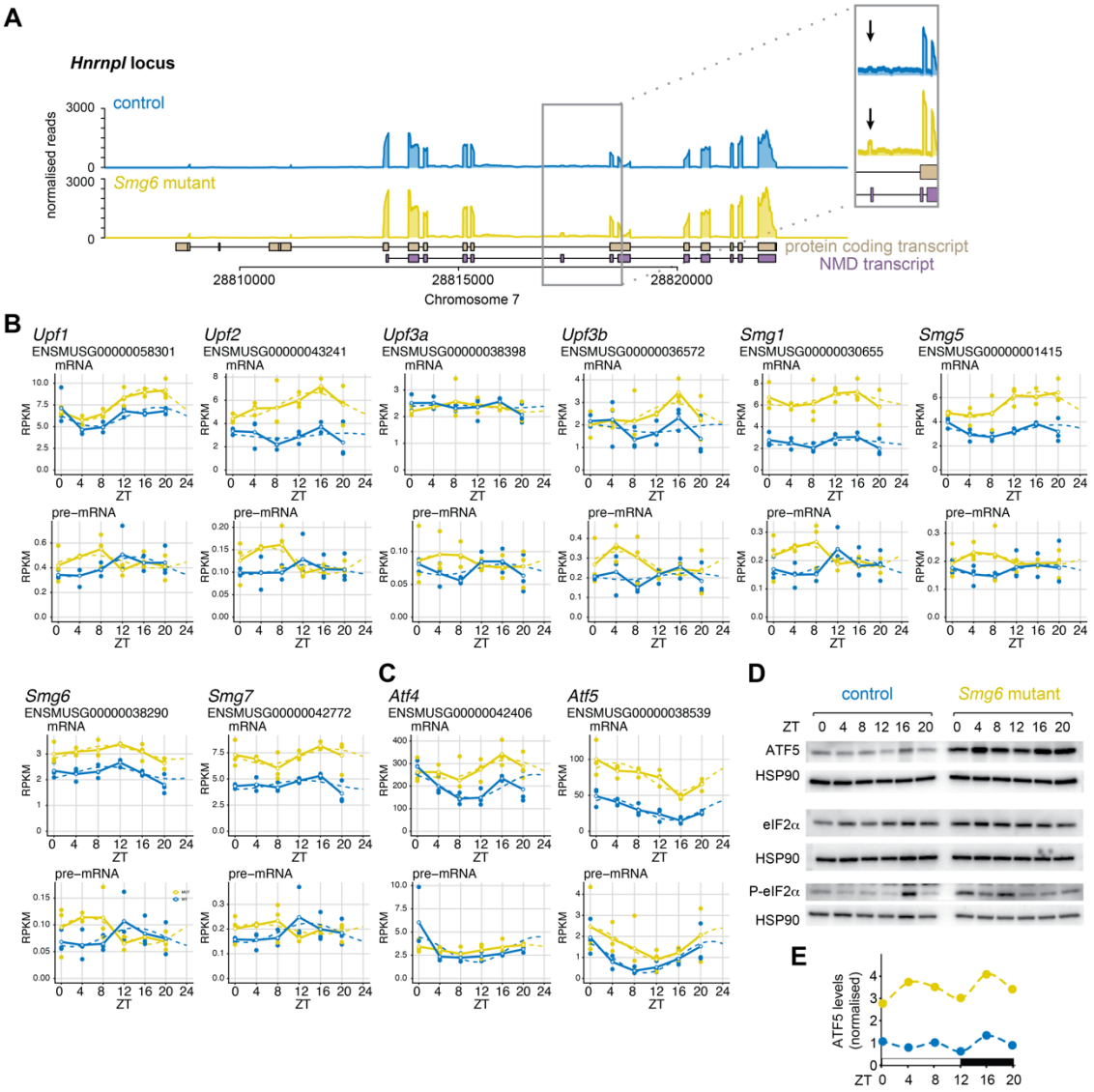

Supplementary Figure S2. (**A**) Read coverage on the *Hnrnpl* locus indicates the specific upregulation of transcript isoforms that are NMD-annotated and that can be identified by specific exons (see arrows in insets) in liver tissue. (**B**) RNA-seq data is plotted for indicated genes – that all encode components of the NMD machinery itself – for mRNA (upper panels; exonic reads) and pre-mRNA (lower panels; intronic reads) for *Smg6* mutants (yellow) and controls (blue). RPKM values of individual animals are shown as dots with solid lines connecting the means for each timepoint. The dashed lines represent the rhythmic data fit using the parameters from MetaCycle. (**C**) RNA-seq data is plotted for *Atf4* and *Atf5* for mRNA (upper panels; exonic reads) and pre-mRNA (lower panels; intronic reads) for *Smg6* mutants (yellow) and controls (blue). RPKM values of individual animals are shown as dots with solid lines connecting the means for each timepoint. The dashed lines represent the rhythmic data fit using the parameters from MetaCycle. (**D**) Western blot analysis of liver tissue (as in Fig. 4D) for ATF5, eIF2α and phospho-eIF2α in *Smg6* mutant and control liver samples; HSP90 served as loading control. (**E**) Quantification of ATF5 signal, normalised to HSP90 as loading control, from Western blot shown in (D).

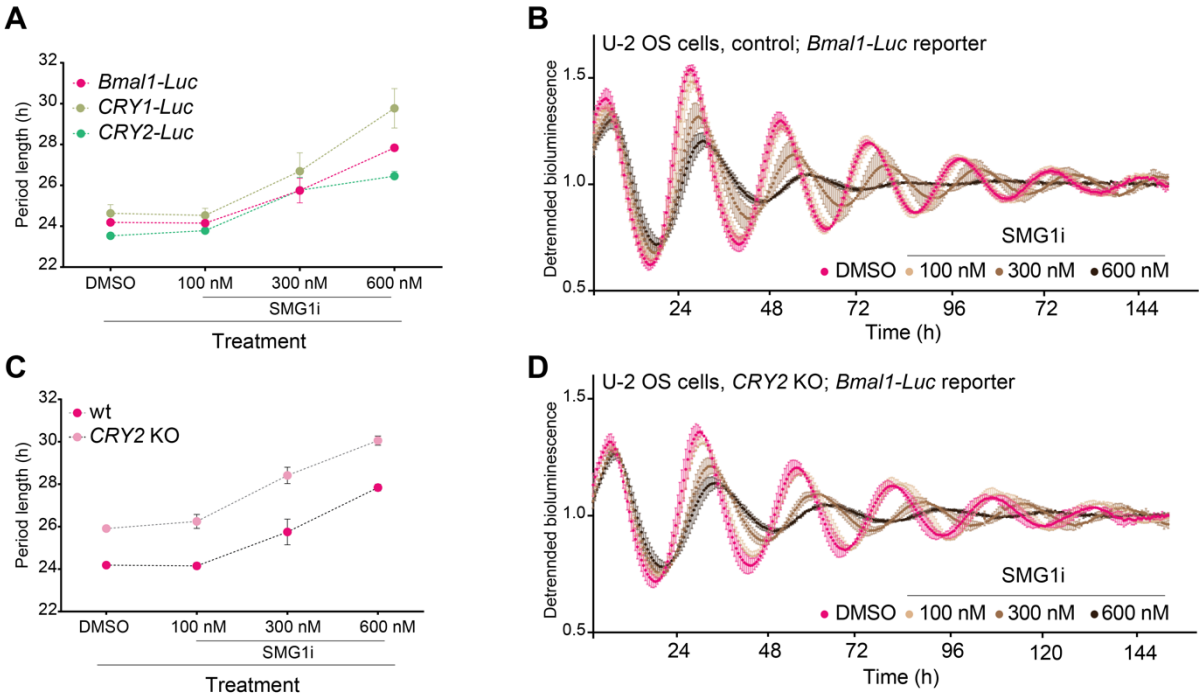

Supplementary Figure S3. Pharmacological NMD inhibition prolongs circadian period in human osteosarcoma U-2 OS cells. (**A**) Period length of the circadian reporters *Bmal1-Luc* (fuchsia), *CRY1-Luc* (khaki) or *CRY2-Luc* (green) in the presence of increasing concentrations of SMG1i or vehicle (DMSO, equal volume as for the highest SMG1i dose). (**B**) Traces of *Bmal1-Luc* detrended bioluminescence signal in wild-type U-2 OS cells treated with increasing dosage of SMG1i or vehicle. Solid circles represent mean, error bars represent standard deviation. (**C**) Period length of the circadian reporter *Bmal1-Luc* in wt (pink) or *CRY2* KO (fuchsia) U-2 OS cells (**D**) Average traces of *Bmal1-Luc* detrended bioluminescence signal in *CRY2* KO U-2 OS cells treated with increasing concentrations of SMG1i or vehicle. Solid circles represent mean, error bars represent standard deviation. *Bmal1-Luc* reporter contains the murine *Arntl/Bmal1* promoter driving firefly luciferase; *CRY1*-Luc and *CRY2*-Luc are fusion protein reporters between the CRY protein and firefly luciferase, generated from the endogenous locus. See Materials and Methods for details.